Revision 3

Word count: 7,779 (Word count including references: 9,103)

Resolving sub-micron-scale zonation of trace elements in quartz using TOF-SIMS.

Ryan North[1], Dominique Tanner[1], Mitchell Nancarrow[2], Bozana Pasic[3] and John A. Mavrogenes[3].

[1]GeoQuest Research Centre, School of Earth, Atmospheric & Life Sciences, University of Wollongong, Wollongong, NSW, 2522, Australia

[2]Electron Microscopy Centre, Australian Institute for Innovative Materials, University of Wollongong, Wollongong, NSW, 2522, Australia

[3]Research School of Earth Sciences, Australian National University, Canberra, ACT, 0200, Australia

Abstract

Quartz is abundant in the Earth's continental crust and persistent throughout the geological record. Trace element signatures in silica minerals can be used to infer processes operating in magmatic and hydrothermal systems. Conventional analyses of trace elements in silica minerals are limited by either spatial or mass resolution (e.g., wavelength-dispersive X-ray spectroscopy, micro X-ray fluorescence, laser ablation inductively coupled mass spectrometry (LA-ICP-MS), and secondary ion mass spectrometry (SIMS). Time-of-flight SIMS (TOF-SIMS) is a relatively new technique for geological applications and provides both high spatial and mass resolution. This minimally-destructive, in situ technique rapidly acquires a full suite of elements

down to tens of nanometers depth. No previous study has utilized TOF-SIMS to analyse quartz or silica. Four samples of silica minerals representing distinct environments in a magmatic-hydrothermal system were characterized with optical microscopy and qualitative cathodoluminescence (CL), quantitatively analysed for trace elements with 157 nm LA-ICP-MS, and qualitatively mapped for trace elements using TOF-SIMS. The novel technique produced maps of trace element distribution in silica minerals to a maximum resolution of 65 nm and consistently resolved light elements (including Li) to 195 nm. That makes this study the highest resolution geochemical characterization of silica minerals, and places it among the highest resolution analyses by TOF-SIMS, or any technique, for that matter. TOF-SIMS isotope maps differentiate trace elements hosted in nano- and micro-inclusions from lattice incorporation in quartz and cryptocrystalline silica – an impossibility for lower resolution techniques, allowing insights into cations substituting for Si^{4+} in the crystal lattice and their role in activating CL in low-temperature epithermal quartz. Further development of this technique could see TOF-SIMS become a routine tool for measuring diffusion profiles in a range of other geological materials. Quantification of TOF-SIMS would revolutionise mineral characterisation, especially given its temporal efficiency and low sampling volume.

Key words:

TOF-SIMS; quartz; trace element; in situ; silica.

Introduction

Quartz is ubiquitous throughout the Earth's continental crust, deposited in a diverse array of igneous, metamorphic, sedimentary and hydrothermal settings. Its abundance and persistence

in the geological record (Taylor and McLennan 1985) make it an ideal candidate to preserve chemical archives in magmatic and hydrothermal systems. Changes in the microstructure and trace element composition of quartz are used to infer the environment of crystallisation (Götze 2009).

Relative to other silicate minerals, quartz hosts a limited range of trace elements in solid solution. Trace elements that substitute into the tetrahedral silicon site in quartz include Ti^{4+} or Ge^{4+}, or trivalent ions such as Al^{3+} or Fe^{3+} coupled with a charge-compensating ion such as K^{+}, Na^{+}, Li^{+}, Cu^{+}, Ag^{+} or H^{+} (Müller et al. 2003; Götze 2009). The combination of trace element incorporation and microstructural defects in quartz give rise to the wide range of intra-crystalline textures visible in cathodoluminescence (CL) imagery. Unlike routine imaging techniques (e.g. transmitted light, reflected light and backscattered electron (BSE) imaging), CL imaging reveals that quartz grains are rarely homogeneous. Quartz grains typically exhibit micrometer to sub-micrometer-scale textures ranging from oscillatory zonation, healed fractures, planar features, streaks or mottled patches depending on their provenance (c.f., Seyedolali et al. 1997; Bernet and Bassett 2005). However, CL is a qualitative imaging technique that cannot reliably decouple the contribution from multiple trace elements and crystal defects (Müller et al. 2003, 2010; Rusk et al. 2006, 2011; Vasyukova et al. 2013). Therefore, in situ techniques with high spatial resolution are required to analyse the trace element signature of most quartz grains.

While quartz hosts a limited range of trace elements in solid solution, changes in quartz chemistry help petrologists track magmatic and hydrothermal processes (e.g., Breiter et al. 2017; Monnier et al. 2018; Müller et al. 2018; Peterková and Dolejš 2019) and determine the provenance of sediments (e.g., Dennen, 1967; Götze and Zimmerle, 2000; Götze, 2009; Müller and Knies, 2013; Ackerson et al., 2015). In magmatic systems, quartz chemistry elucidates

crystallisation temperatures, pressures and fluid compositions (Müller et al. 2018) as well as recording the origin and evolution of pegmatites (Larsen et al. 2004). In hydrothermal systems, trace elements in quartz provide one of the few independent geothermometers (Wark and Watson 2006) and track fluid chemistry (Penniston-Dorland 2001; Rusk et al. 2006; Breiter et al. 2017; Monnier et al. 2018). Titanium in quartz is not only used for geothermometry; gradients in the Ti content across quartz phenocrysts also permit geospeedometry, used to infer timescales of magmatic-hydrothermal activity in porphyry copper deposits (Cernuschi et al. 2018). Provenance studies have utilized the trace element composition of quartz to constrain marine sediment sources (Dennen 1967; Müller and Knies 2013), though provenance can also be interpreted from quartz using various other physical and chemical properties (Götze and Zimmerle 2000).

While the trace element chemistry of quartz has numerous petrological applications, these analyses are significantly less common than those of other silicate minerals (e.g. olivine, pyroxenes, feldspars). In part, this is because quartz does not exhibit solid solution and impurities typically occur at low concentrations (Götze 2009). Another reason for the relative lack of publications reporting trace element concentrations in quartz is the technical difficulty. Routine X-ray techniques with high spatial resolution (wavelength dispersive spectrometry and micro X-ray fluorescence) are unable to detect the light cations which substitute into the quartz lattice (e.g., H, Li, Be, B). Electron probe microanalysis (EPMA) is capable of resolving trace elements in quartz >B to parts per million (ppm) concentrations with sufficient spatial resolution to differentiate between zones (i.e., spot size 5 μm; Müller et al. 2003), but is limited by the number of spectrometers, so that typically only five elements can be measured simultaneously. Energy dispersive spectroscopy (EDS) is not limited in the number of elements it can measure at a given time but is not capable of measuring minor or trace elements, so it is rarely used to

93 analyse quartz. Mass spectrometry techniques such as laser ablation-inductively coupled plasma-
94 mass spectrometry (LA-ICP-MS) and secondary ionization mass spectrometry (SIMS) are
95 capable of analysing Li-U in situ (or the full range of elements in the case of SIMS), but require
96 relatively large sampling volumes (i.e., up to 250,000 μm^3 and 5,000 μm^3 respectively; Müller et
97 al. 2003) resulting in blurred or averaged results across crystal zones (Müller et al. 2003; Götze
98 2009). Most LA-ICP-MS systems used in the Earth science use a 193 nm laser, which does not
99 couple well with the quartz lattice (Chenery and Cook, 1993). This causes irregular ablation of
100 quartz, resulting in the infrequent ablation of large quartz chips that produce poor-quality data.
101 NanoSIMS has been used to measure semi-quantitative Ti variations in quartz at spatial scales as
102 fine as ~650 nm (Seitz et al. 2018) demonstrating its ability as one of the only techniques
103 currently available to resolve intra-crystalline heterogeneity at sub-micrometer scales.

104 Time-of-flight-secondary ionization mass spectrometry (TOF-SIMS) using a dual-beam
105 electron microscope is a relatively new technique in petrology that overcomes many of the
106 current limitations of available analytical techniques to ablate quartz. At its current capability,
107 TOF-SIMS can provide in situ qualitative isotopic maps of multiple trace elements at the parts
108 per million level achieving sub-micrometer resolution in geological materials (e.g., Pabst et al.
109 2011; Gaillou et al. 2012; Montalvo et al. 2019).

110 TOF-SIMS has been used to analyse a few common rock-forming minerals to provide the
111 analytical and spatial resolution necessary for a range of petrological applications, especially
112 those including light elements. The majority of these analyses are qualitative, but one study of B
113 in diamond reports quantitative measurements (Gaillou et al. 2012). So far, qualitative TOF-
114 SIMS has been used to analyse OH in lunar fluorapatite (McCubbin et al. 2010), Li and B in
115 serpentinite (Pabst et al. 2011), pyroxene (Saunders et al., 2012) and reidite geochemistry

(Montalvo et al. 2019), as well as a range of synthetic materials. But until now, no study has used the TOF-SIMS technique to measure the trace element distributions in quartz or cryptocrystalline silica.

Here, we use the novel TOF-SIMS technique on a dual-beam (field-emission electron beam and a gallium ion beam) electron microscope to resolve elemental heterogeneity in silica minerals on a sub-micrometer scale. Samples were chosen to represent the spectrum of formation conditions in magmatic-hydrothermal systems as they exhibit distinct growth patterns. We assess the analytical capabilities and spatial resolution of the technique for quartz and cryptocrystalline silica by coupling qualitative TOF-SIMS analyses with CL maps and adjacent 157 nm LA-ICP-MS traverses.

Samples and localities

Natural silica samples from four magmatic-hydrothermal systems were selected for analysis (Figure 1), trimmed, cast into resin blocks and polished. Their environments of formation are illustrated in Figure 2.

Cryptocrystalline silica from a low-sulfidation epithermal Au-Ag-Cu-Pb-Zn deposit (EPI-CS)

A small chip of laminated botryoidal cryptocrystalline silica (Figure 1a) was sourced from the adularia-sericite Crofoot-Lewis epithermal Au-Ag deposit in Nevada (c.f., Ebert and Rye 1997). The sample contains botryoidal translucent milky silica encrusting opaque white silica containing vugs. This sample represents typical cryptocrystalline silica from a low-sulfidation environment. Results from Raman spectroscopy (Supplementary Figure 1) suggest at

least three distinct structural phases of cryptocrystalline silica in this sample. Raman spectra collected for this sample from the same analytical area as CL microscopy, LA-ICP-MS and TOF-SIMS is most similar to spectra for opal-CT in data from a spectral information database (RRUFF; Lafuente et al. 2016). Though the area may well be opal-CT, correlation of spectra is indicative rather than definitive, and since a variety of phases are present (opal-C, opal-A), this sample will be referred to as cryptocrystalline silica.

Quartz from a low-sulfidation epithermal Au-Ag deposit (EPI-Q)

A small fragment of epithermal sinter containing quartz microcrystals (Figure 1b) was sourced from a low temperature, low sulfidation silica sinter terrace in the Silverton Mining Area, Colorado (Varnes 1963). This microcrystalline quartz is associated with minor adularia, pyrite and apatite, and is typical of quartz from a low-sulfidation epithermal setting.

Quartz from a cassiterite-bearing greisen (GREI-Q)

A small chip from a vein containing 1-5 mm quartz crystals and 2 mm cassiterite crystals (Figure 1c) was selected from the Cligga Head Sn-W greisen deposit in Cornwall, UK. This sample represents the most fractionated, high-temperature hydrothermal end-member of quartz in magmatic-hydrothermal systems.

Quartz within a unidirectional solidification texture (UST-Q)

A small fragment of porphyritic green aplite intergrown with bands of quartz displaying uni-directional solidification texture (UST) was selected for this study (Figure 1d). This sample was collected from the Kidston open pit Au mine located in Queensland, Australia (c.f., Figure

3a in Baker and Andrew 1991). This sample is interpreted to form from fluctuations in pH_2O during rhyolite fractionation causing repeated cycles of fluid exsolution where prismatic quartz is deposited, with terminations pointing in towards the magma reservoir. Thus, the UST quartz in this study represents the most magmatic end-member of hydrothermal quartz in magmatic-hydrothermal systems.

Methods

Sample characterization

Each polished sample was imaged under reflected light to identify mineral phases, regions of interest and topographical defects. Raman spectroscopy was used to distinguish the exact silica phase in the cryptocrystalline silica sample. Trace element concentrations were acquired with LA-ICP-MS across a transect in each sample, then CL images and TOF-SIMS analyses were undertaken adjacent to each transect to compare quantitative LA-ICP-MS data and qualitative TOF-SIMS images.

Raman spectroscopy

Raman spectra were collected for the cryptocrystalline silica sample using a WITec Alpha 300R confocal Raman microscope equipped with a UHTS spectrometer and a visible DV401 CCD detector, housed at the School of Earth, Atmospheric & Life Sciences, University of Wollongong. The excitation source used was a diode laser operated at a 532 nm wavelength with 38 mW output. Acquired spectra composed of six accumulations with 30 s integration times each using a 50x objective lens, achieving sub-micrometer analytical resolution. Identification of

opal phases involved comparison with Raman spectra from the RRUFF database (RRUFF ID's: R060651, R060652, R060653).

157 nm LA-ICP-MS

The trace element composition of silica samples was quantified using a Varian 820 quadrupole ICP-MS coupled to a 157 nm F_2 Helex laser ablation system housed at the Research School of Earth Sciences, Australian National University. Use of a 157 nm wavelength laser eliminates occasional issues associated with 193 nm wavelength lasers, where irregular ablation occurs in transparent quartz due to poor lattice coupling with the laser (Chenery and Cook 1993). Trace element concentrations were determined using ~500 – 2000 μm traverses using a ~100 μm-diameter spot. Analyses were collected at a pulse rate of 10 Hz with 100% mirror. The ICP-MS was tuned to low oxide production rates and analyses were only conducted >40 minutes after sample change, to minimize oxide production rate and background counts. Data were reduced using an in-house spreadsheet, with NIST 610 used as the bracketing external standard. A value of 46.74 wt% ^{29}Si was used as the internal standard.

Cathodoluminescence imaging

Panchromatic CL images were acquired at 15 kV under high vacuum with a load current ~50 μA using a JEOL JSM-6610A SEM with a Robinson CL detector housed at the Research School of Earth Sciences, Australian National University. These images were taken at a broad scale so that areas representative of internal growth textures could be highlighted for comparison with TOF-SIMS element maps. Color-filtered CL images were obtained using a Gatan MonoCL4 detector attached to a JEOL 6490LV SEM housed at the Electron Microscopy Centre

at the University of Wollongong. These analyses were collected under low vacuum at 5 kV with a dwell time of 1 ms to maximize data collection efficiency and avoid bleaching. Areas for color-filtered CL imaging were positioned adjacent to the LA-ICP-MS ablation line so that known element concentration values could be spatially correlated. Filters for red, green, blue and white (panchromatic) light were inserted consecutively to filter light emitted during cathodoluminescence imaging. The order was chosen to minimize bleaching effects to the sample.

TOF-SIMS

Qualitative isotope abundance maps were acquired with a TOF-SIMS unit attached to an FEI Helios NanoLab G3 CX dual beam (electron and ion beam) microscope at the Electron Microscopy Centre, University of Wollongong. The dual beam microscope originates from FEI's factory in Brno, Czech Republic and the SIMS is manufactured by TOF-Werk in Thun, Switzerland. Each polished mount was air plasma cleaned and coated with 50 nm of gold prior to analysis. Samples were ablated using Ga^+ at 30 kV with a 230 pA beam current and 10 ms dwell time. Two-dimensional 100 x 150 μm raster areas of 512 x 768 spots (2x binned down in software) were analysed and stacked to create a three-dimensional dataset for each isotope. This stack is estimated to represent tens of nanometers depth based off FIB milling rates in monocrystalline silicon (Rubanov and Munroe 2004). However, the exact depth of material that is removed is difficult to quantify and comparison to previous studies are unproductive due to the variety of matrix effects and operating conditions.

Areas of 50, 75, 200, 500 and 800 μm lengths on the longest dimension were also tested with the same spot resolution. Data were obtained for positive ions of isotopes with atomic mass

230 units between 6 and 200. Isobaric mass interferences commonly involved isotopes of the major
231 elements in silica minerals as well as Ga and Au contamination from the beam source and
232 conductive coating, respectively. In the case of an interference, alternative isotopes of that
233 element were investigated. Potential mass interferences relevant to silica minerals are listed in
234 Supplementary Table 1.

235 From the three-dimensional stack of two-dimensional isotope maps, a representative
236 section was acquired. Sections were bound by depths where anomalies from the gold coating are
237 eliminated but charging effects are not yet apparent (Figure 3). Where possible, TOF-SIMS
238 analyses were undertaken within the area of the CL analysis, adjacent to the LA-ICP-MS line.

239 Maps were processed to highlight element variation and exclude anomalies from
240 topographic defects. Outliers were removed according to a threshold unique to each image.
241 Smoothing was applied by duplicating the image, applying a median filter to each pixel in one
242 image, then averaging pixel values from the filtered and unfiltered copies. This method smooths
243 overall element trends while retaining significant but spatially limited high values. If vignetting
244 was apparent due to detector fall-off, a large-scale Gaussian blur was applied to another
245 duplicate and resulting pixel values subtracted from the final image.

246 Relative intensity transects were produced by averaging pixel values along the y-axis to
247 create a ~3 μm bar. This provides a more accurate representation of relative concentration
248 without compromising resolution. By averaging pixel values in a small area parallel to crystal
249 zones, mixing of oscillatory zones is not an issue. This process was repeated for corresponding
250 CL maps. A running mean was applied to data for CL and TOF-SIMS transects to enhance
251 comprehension of trends.

252

253 # Results

254 ## 157 nm LA-ICP-MS

255 LA-ICP-MS results reveal the concentration of trace elements along ~100 um-wide
256 traverses in each sample. To characterise each region of interest in this study, the minimum,
257 maximum, and median values from LA-ICP-MS traverses are provided in Table 1. In each
258 sample, Al is the most abundant trace element, followed by either K, Na or Ca. Figure 4 shows
259 the range and distribution of measured elements for each traverse, ordered by decreasing median
260 value. These results are compiled from the full length of each LA-ICP-MS traverse, and thus
261 may include fluid and/or mineral inclusions within each sample.

262 Time-resolved analyses of LA-ICP-MS data (Supplementary Table 2) demonstrate that
263 trace elements are either consistently above detection across a traverse, locally concentrated, or
264 mostly below detection. The spatial distribution of trace elements across the region of interest in
265 each sample is presented in Supplementary Figures 2-5 and summarised in Table 2. In each
266 sample, Al is positively correlated with one or more of K, Li and Na. Further, the $\sum 3+$ cations
267 per formula unit and $\sum 1+$ cations per formula unit positively correlate across each traverse
268 (Figure 5) while the $\sum 3+$ cations and $\sum 4+$ cations do not. Note that the ratio between $\sum 1+$ and
269 $\sum 3+$ cations in cryptocrystalline silica is closer to 2:3 than 1:3 as observed in quartz samples.

270

271 ## Cathodoluminescence (CL) imaging

272 Micrometer-scale heterogeneity is present in each of the four samples highlighted by
273 panchromatic CL images in Figure 6. The CL signal in all samples is dominated by blue
274 wavelengths, with relatively minor contributions from green and red (Supplementary Figure 6).

EPI-CS (Figure 6a) shows two distinct textures most visible in panchromatic CL. Botryoidal contacts delineate coarse, dark laminations from more finely laminated silica with greater variation in CL intensity. Blue light emission contributes to most of the CL, though some very faint structures can be distinguished in green CL. No variation is visible in red. Note that compared to the other samples, the overall CL intensity is much weaker.

EPI-Q (Figure 6b) displays distinct euhedral crystal structures with oscillatory zones. These euhedral crystals luminesce strongly in blue wavelengths and weakly in green wavelengths, but not red wavelengths.

GREI-Q (Figure 6c) shows a network of irregular dark veins cross-cutting oscillatory and sector zones in panchromatic CL. The texture is similar to that observed in UST-Q. Color filtered results were not acquired for this sample.

UST-Q (Figure 6d) sample exhibits large sector zones interrupted by an irregular network of lower signal CL micro-veins. Within some sector zones, CL is homogeneous. Blue wavelengths contribute to most of the overall CL signal, though a few micrometer-scale spots emit a strong green signal often within or adjacent to micro-veins.

TOF-SIMS

Trace element distribution

A map was created for isotope abundances of nominal masses 6 – 200, yet only ^{7}Li, ^{23}Na, ^{27}Al, ^{28}Si, ^{39}K and ^{40}Ca returned measurements above the signal to noise threshold. Processed isotope maps for ^{7}Li, ^{23}Na, ^{27}Al, ^{39}K and ^{40}Ca for UST-Q, GREI-Q, EPI-Q and EPI-CS are presented in Figures 7, 8, 9 and 10, respectively, alongside the ^{28}Si map which effectively shows surface topography. Each map shows the relative concentration of each isotope. Note that Ti was

298 not recorded above the signal to noise threshold in any sample, despite being present at up to 71
299 ppm in LA-ICP-MS analyses.

300 The distribution of trace elements in EPI-CS (Figure 7) is largely controlled by botryoidal
301 zones. Aluminium, K and Na are present and positively correlated in both micrometer-scale
302 botryoidal edges and irregular, sporadic micro-clusters. Calcium also appears in the irregular
303 clusters but is not concentrated in the botryoidal lamination. Lithium in EPI-CS was only
304 detected in the botryoidal lamination.

305 The distribution of Al, K, Li, Na and Ca in the EPI-Q sample (Figure 8) are primarily
306 controlled by euhedral, oscillatory growth zones. The distribution of K is well defined and
307 concentrated mostly on oscillatory zone boundaries. Notably, even within single oscillatory
308 zones the distribution of K is heterogeneous. Sodium positively correlates with K, however
309 variation in Al is not completely coupled with Na and K. In this sample, Al has a similar
310 distribution as Li, which is relatively homogeneous, but not necessarily diffuse, as highlighted by
311 the clear oscillatory zone of low concentration. Micrometer-scale Si voids are associated with
312 high Al, K, Na, and Ca concentrations but low Li concentrations. In EPI-Q, Si voids are gaps
313 between microcrystals.

314 In GREI-Q (Figure 9), the TOF-SIMS maps display a similar mosaic-like texture visible
315 in some CL (Supplementary Figure 6), but do not record the network of secondary veins or
316 characteristic oscillatory and sector zoning (Figure 6). Most of the trace element distribution is
317 controlled by micrometer-scale voids in Si, where Na, Ca and K are concentrated. Aluminium
318 appears to be present in some of these voids but is predominantly correlated with Si. In GREI-Q,
319 Si voids and the resulting surface artefacts are most likely the product of fluid inclusions exposed
320 during sample polishing. Some spherical voids in the silica that host Al and K (an example of

which is labelled in Figure 9) are contained below the sample surface as indicated by TOF-SIMS depth profiles (Supplementary Figure 7). The distribution of Li is relatively diffuse and less affected by surface roughness. Vignetting is apparent in Si and Al maps due to detector falloff in analyses at this scale (500 μm width).

The distribution of trace elements in UST-Q (Figure 10) is similar to the pattern of healed microfractures observed under CL. Alumnium, K, Na and Ca are distributed heterogeneously throughout quartz in regions of bright, apparently homogeneous CL. These bright regions contain Al and K, locally concentrated within nanometer-scale clusters. When Al and K maps are overlaid, these nano-clusters align perfectly, suggesting these clusters are not noise. Note that K show more clustering than Al. At the top left corner of the Al and K maps, a greater concentration of nano-clusters can be seen. Sodium and Ca appear mostly homogeneous in this region, with sparse, locally concentrated nano- and microscale clusters. When overlaid, Ca nano-clusters align with those of Na, though some Na nano-clusters align with K. Microscale clusters are associated with visible Si voids. The bright regions in CL bearing Al, K, Na and Ca are crosscut by secondary veinlets low in trace elements. Linear low-Ca features are present in UST-Q that do not correlate with the veinlets visible in Al and K. Faint lineations visible in the Na and Ca maps are surface artefacts from repolishing an area previously analysed with TOF-SIMS. They are not an inherent feature of the quartz. Li was not recorded above the noise threshold in UST-Q where it is present at ~1 ppm (Figure 4, Supplementary Figure 5).

Analytical parameters and resolution

A range of analytical parameters were varied to maximize sensitivity and spatial resolution of isotope maps, without degrading the surface coating so much that charging effects

inhibited collection. The finest scale analysis was conducted over a 50 μm width on the UST-Q sample (Figure 11), recording data with a sampling spot diameter less than 65 nm. At beam currents of 230 pA the 50 μm analysis perforated the conductive gold coating much quicker than broader scale analyses, thereby reducing the available depth to create isotope maps, and reducing the signal above the noise threshold. This beam current, however, still produced more signal than longer analyses at lesser beam currents (i.e. 80 pA or 40 pA).

At the finest scale, only data for Si and trace elements Al, K, Na and Ca produced signal above the noise threshold in UST-Q. These are the most abundant elements in UST-Q (Figure 4). The region of quartz analysed is largely featureless (Figure 11) but demonstrates the spatial resolution of the technique as it resolves nanometer-scale clusters of Al and K concentrated in surface defects and Si voids. The finest scale that Li could be reliably detected on was in 150 μm width maps of EPI-Q which have sampling spot diameters less than 195 nm diameter.

Discussion

Spatial resolution of TOF-SIMS

As highlighted by similar studies of in situ quartz geochemistry, the analysis area and volume of conventional techniques such as EPMA and LA-ICP-MS are often too coarse to resolve true geochemical heterogeneity in zoned crystals (Perny et al. 1992; Müller et al. 2003, 2008). LA-ICP-MS requires analysis volumes on the order of ~200,000 μm^3, SIMS can analyze smaller volumes of material (~3,000 μm^3), and while EPMA can analyze even smaller volumes (~150 μm^3) in less than 5 μm diameter spots (Müller et al. 2003), TOF-SIMS is capable of mapping minerals at a sub-micrometer scale with sufficient analytical resolution to detect trace

366 elements. Like other in situ microbeam techniques, data quality from TOF-SIMS is limited by
367 surface roughness and the level of contamination during sample preparation.

368 TOF-SIMS maps of silica minerals in this study consistently recorded valid
369 measurements for trace elements, notably including the light element Li, with a spatial resolution
370 of 195 nm. In the EPI-CS sample, Li was detected when LA-ICP-MS measurements indicate its
371 concentration to be at most 15 ppm within the analytical volume of the technique. The highest
372 effective spatial resolution of 65 nm was achieved in a 50 μm width analysis of the UST-Q
373 sample, though at this scale the technique was only sensitive to the more abundant elements Al,
374 K, Na, and Ca. This is comparable to the highest spatial resolution recorded by the other
375 geological studies that utilise TOF-SIMS (60 nm; Montalvo et al. 2019), although <50 nm lateral
376 resolution has been achieved in a synthetic standard (Alberts et al. 2014).

377

378 **Sensitivity of TOF-SIMS to trace elements in quartz and silica**

379 TOF-SIMS was able to obtain qualitative maps to assess Si, Al, K, Li, Na and Ca
380 distribution in the quartz samples studied. The samples were known to exhibit reasonably high
381 concentrations of other trace elements (e.g., Ti, B, Sr, Mg, Mn, Sb; Table 1) that were not
382 observed by TOF-SIMS. Particularly of note, TOF-SIMS did not detect Ti in quartz, even when
383 present at up to 71 ppm (UST-Q sample). Similarly, Fe, a common trace element in quartz, was
384 unable to be measured by TOF-SIMS. This may be due to LA-ICP-MS analyses measuring
385 volumes much greater than the surface sensitive technique TOF-SIMS (and thus incorporating
386 micro-inclusions) but is more likely due to the limits of detection in TOF-SIMS of these
387 elements in quartz. The detection limits are a function of concentration, ionisation potential and

388 matrix effects, though more research needs to be undertaken to optimise detection of useful trace
389 elements in quartz and silica with TOF-SIMS.
390
391 **Distribution of trace elements in quartz and silica**
392 TOF-SIMS allows the detection of trace elements in quartz on finer scales than was
393 previously possible, providing insight into whether elements are incorporated into the crystal
394 lattice or are hosted within micro-inclusions. Evidence for both lattice incorporation and isolated
395 nano- and/or micro-inclusions were observed that would not have been possible with less
396 spatially precise techniques. The nature of element partitioning in quartz is summarised in Table
397 3 by sample type (i.e., environment of formation). Relatively homogeneous distributions of trace
398 elements in TOF-SIMS maps, especially those that correlate with Si, are interpreted as residing
399 within the lattice. Nanometer-scale localised concentration clusters where Si appears
400 homogeneous are interpreted as nanoscale mineral inclusions, while high concentration clusters
401 correlating with Si voids are interpreted as surface contamination from polishing. For example,
402 Al in EPI-Q (Figure 8) is lattice bound, while Al and K in UST-Q (Figure 10) are hosted by
403 nano-inclusions where Si is homogeneous. The irregular texture of sporadic trace element micro-
404 clusters in EPI-CS (Figure 7) may be controlled by silica morphologies such as bumpy
405 microspheres or clustered nanospheres (Lynne et al. 2007). EPI-Q, GREI-Q and UST-Q all
406 feature some surface contamination in Si voids (Figures 8, 9 and 10, respectively).
407 These interpretations can be correlated with the LA-ICP-MS traverses on the same
408 samples, and whether Al, K, Li and Na were consistently above detection or were locally
409 concentrated (Table 2). Signals for Ca was consistently below background noise in all laser
410 ablation traverses, so correlation is not possible in these samples. In all samples, the

aforementioned elements were above detection and varied on the tens to hundreds of micrometer-scales, but TOF-SIMS maps were able to elucidate that Al, Ca, K, Li and Na are often present as nanometer-scale silicate mineral inclusions (e.g., Figure 10), micrometer-scale fluid inclusions (e.g., Figure 9) or surface contamination (e.g., Figures 8, 9 and 11) rather than in silica lattice. The difference in volume of ablation gives rise to this discrepancy. Nano-inclusions may actually represent transitional lattice defect/nano-inclusion clusters (Müller et al. 2003) and could be characterised further with atom probe tomography or transmission electron microscopy, though this was beyond the scope of this initial study.

Relationship of charge balancing cations in quartz and silica

As observed in both the LA-ICP-MS and TOF-SIMS data, some elements incorporated into the quartz lattice are spatially correlated. Considering only the LA-ICP-MS traverses, results show that Al is positively correlated with one or a combination of K, Li and Na in each sample. Also, the correlation between ∑3+ cations per formula unit and ∑1+ cations per formula unit (Figure 5) supports observations in the literature of K^+, Li^+ and Na^+ acting as charge balancing cations for Al^{3+} substituting into Si^{4+} sites in quartz (Müller et al. 2003; Götze 2009). However, we note a systematic difference between the ratio of ∑1+ cations to ∑3+ cations in cryptocrystalline silica (2:3) and quartz (1:3; Figure 5). Though unmeasurable by techniques used here, H^+ ions likely also contribute to balancing charge, especially in the more magmatic end-members (Müller and Koch-Müller 2009).

If K^+, Na^+ and Li^+ are assumed to be the dominant charge balancing ions for Al^{3+}, the contribution of each element varies between quartz samples (Figure 12). The dominant balancing cations for the most magmatic end-member UST-Q are K^+ and Na^+, while Al^{3+} in GREI-Q is

434 balanced by Na^+, Li^+ and some K^+. Minor Al^{3+} in the epithermal sample EPI-Q is predominantly
435 balanced by Li^+ and K^+, while in EPI-CS it is balanced by Na^+ and K^+. Only in one sample (EPI-
436 Q) can the contribution of the charge balancing cations Li^+ and K^+ be spatially differentiated
437 along the LA-ICP-MS traverse (Supplementary Figure 3). These relationships may have
438 implications for provenance determination, providing an alternative to the Ti-Ge-Al ratios
439 proposed by Götze (2009) which are ineffective with in situ data (Tanner et al. 2013).

440 The relationships between these elements become more complex when considering the
441 TOF-SIMS maps. The EPI-Q isotope maps confirm that K and Na spatially correlate with Al, but
442 only within fine oscillatory zones, while Li correlates with Al over a broader area (Figure 8). In
443 this sample, even single oscillatory zones contain a homogeneous distribution of K and Na.
444 Similar behavior is observed in EPI-CS (Figure 7), where Al, K and Na are correlated, but Li is
445 only apparently correlated with Al at botryoidal zone boundaries. In isotope maps of GREI-Q
446 (Figure 7), Li has a similar distribution to Al while Na is negatively correlated and only found in
447 micro-inclusions. Potassium in the same sample is located within both the quartz matrix and
448 inclusions. In UST-Q, K is strongly correlated with Al, but only with Na and Ca in inclusions
449 associated with voids in Si.

450 The complex spatial distribution of charge balancing cations in quartz, and the
451 heterogeneity obscured within single oscillatory zones, could result from the different
452 diffusivities between the monovalent cations, or their partitioning behavior. The high spatial
453 resolution TOF-SIMS maps highlight a more complex geochemical evolution for these samples
454 than could possibly be observed by the analytical scale of LA-ICP-MS.

455

456 **Characterizing cathodoluminescence activators in silica**

Variations in CL textures and colors of quartz crystals are thought to be caused by oxygen vacancies, trace element substitutions and/or intrinsic defects in the crystal lattice (Weil 1984; Müller et al. 2003; Götze 2009; Stevens-Kalceff 2009). Given that TOF-SIMS provides data with high enough spatial resolution high enough for comparison with CL images it could be used to identify which trace elements give rise to CL in quartz.

Studies have found that the cause of blue CL, which contributes substantially to the overall CL signal in quartz, can be related to Ti impurities in the crystal lattice (Sprunt 1981; Müller et al. 2002; Rusk et al. 2008). The inability of TOF-SIMS to resolve Ti concentrations in this study leaves this possibility open. In low temperature hydrothermal quartz with low Ti contents, high concentrations of Al are correlated with darker CL (Rusk et al. 2008).

Relative intensity values along paired transects in CL and TOF-SIMS maps are compared for the low temperature, Ti-poor EPI-Q sample (Figure 13). Results show that while the Al signal in TOF-SIMS remains relatively stable across alternating dark and light CL zones, the proportion of charge balancing cations generally increase in darker CL zones, particularly K. This suggests that the coupling of M^+ (where M is Li, Na, or K) inhibits luminescence in low temperature epithermal quartz. In brighter regions where there is no apparent increase in M^+ ions, Al may be coupled with H^+ as a charge compensator. TOF-SIMS reveals that the high Al-dark CL relationship observed by Rusk et al. (2008) may actually have more dependence on the charge compensating ion for low temperature epithermal quartz. Note that the interaction volume of the electron beam for CL is much larger than that of the ion beam for TOF-SIMS, which will lead to apparently shifted zone boundaries, though this effect is small. Hence, interpretations here should be taken as cursory, requiring further analysis.

Given the variety of factors that influence CL textures and colors in quartz, and the range of paragenetic histories, a 'one size fits all' model may never fully explain hydrothermal quartz. However, strong spatial correlations between textures in CL and trace elements mapped by TOF-SIMS add to the literature by suggesting that charge compensating cations are among the range of luminescence activators.

Analytical considerations and ideal conditions

Quality TOF-SIMS data were the result of a honed methodology involving attention during sample preparation and refined acquisition conditions, such as beam current, grid spacing, and focus. Ideally, samples are polished to near-nanometer overall roughness as TOF-SIMS is a surface sensitive technique. Fine surficial defects such as fluid inclusions opened during polishing are best avoided. Fine surface defects cause glancing angles resulting in greater ablation per ion impact, artificially enhancing signal from the elements present. Topographic pits can also trap contamination from residual polishing media. Note that samples may appear well polished with optical microscopy but can still feature many surface defects at micrometer scales (as in the case of GREI-Q). In cases where surface defects are shallow, clipping the surficial frames of TOF-SIMS data in the Z-dimension can eliminate this problem (Figure 3). Investigating data in cross-section also allows discrimination between trace elements native to the sample (e.g., in fluid or mineral inclusions) from foreign elements concentrated in surface pits (see Supplementary Figure 7). Furthermore, a mount polished to an angle less than horizontal reduces signal collection, an effect previously described for TOF-SIMS (Saunders et al. 2012; Whitby et al. 2012). We also recommend air drying samples completely before

applying conductive coatings as the integrity of the coating deteriorates rapidly with trapped moisture.

A narrow range, or 'sweet spot' of beam current and grid spacing were determined. Large beam currents produced more signal but perforated the conductive coating too quickly, advancing sample charging and inhibiting further analysis of the same location without repolishing. Higher beam currents could be used by increasing the ratio of analysis area to sampling spot size. To obtain high spatial resolution data without premature conductive coating breakdown, the optimum ratio of spot size to step size in gold coated quartz is 130 nm spots with a 50 nm step size at 230 pA (Figure 14a). This grid spacing assumes a well-focussed primary ion beam to maintain conductive coating integrity. Well-focussed and poorly-focussed sampling spot grids are compared beside a collapsed grid in Figure 14. Utilising electron beam charge neutralisation would remove the need for conductive coatings and improve resolution substantially, but the focused ion beam-SIMS system used here was constrained by detector geometry.

TOF-SIMS is an effective qualitative tool to map fine scale geochemical trends in minerals such as quartz but would benefit from quantification. Absolute concentrations of trace elements acquired with TOF-SIMS would remove the need for supplementary quantitative techniques (e.g., LA-ICP-MS) and improve temporal and fiscal efficiency. Gaillou et al. (2012) highlighted the need for adequate standards for TOF-SIMS quantification. Moreover, consistency between analyses in this study was limited by a semi-quantitative z-axis scale in 'frames' rather than nanometers. This prevented analysis of the same volumes of sample, unless it is assumed that all quartz and cryptocrystalline silica samples ablate at the same rate. This assumption is invalid across analyses of different minerals.

524

525 **Implications**

526 This is the first study to apply TOF-SIMS to quartz and cryptocrystalline silica and adds
527 to the limited literature of the technique's geological applications. Results highlight the ability of
528 TOF-SIMS to resolve light elements, including Li between 1 – 15 ppm, in silica minerals at
529 spatial resolutions more precise than other in situ techniques, such as LA-ICP-MS, SIMS and
530 EPMA. Notably, Ti was not able to be detected by TOF-SIMS in this study, and further
531 development of the technique should investigate vacuum contamination, matrix effects or beam
532 sources as the cause of this problem. To our knowledge, the measurement of trace elements to 65
533 nm precision marks the highest resolution analysis of any study of silica, and among the highest
534 resolution TOF-SIMS applications to the Earth sciences.

535 Given the ubiquity of quartz and its function as a geological archive, high resolution trace
536 element maps provided by TOF-SIMS can benefit those reconstructing the physical and chemical
537 conditions of magmatic-hydrothermal systems. Results from TOF-SIMS maps in this study
538 indicate that the nature and distribution of trace elements in quartz is more complex than
539 conventional in situ techniques reveal.

540 TOF-SIMS would prove useful in future studies of silica minerals, as well as other
541 minerals and rocks, to understand CL processes, track diffusion of trace elements, characterize
542 weathering rinds, and potentially provide information about the history of archaeological
543 artefacts such as stone tools. In synthetic materials similar to silica the technique could be
544 applied to image dopant distribution in semi-conductive or advanced materials, or map chemical
545 degradation of smartphone screens. While beyond the scope of this study, quantification of TOF-
546 SIMS analyses would allow quicker and simpler workflows by reducing the need for LA-ICP-

MS coupling. Progress towards quantification would require well characterised, matrix-matched silica mineral standards. Even without quantification, the tool is particularly advantageous in qualitative, time sensitive studies requiring high spatial precision and minimal sample destruction – especially since the add-on TOF-SIMS unit is more accessible than dedicated SIMS instruments.

Acknowledgements

This research used equipment funded by the Australian Research Council (ARC) Linkage, Infrastructure, Equipment and Facilities (LIEF) grant (LE160100063) located at the UOW Electron Microscopy Centre. D.T. acknowledges support from a GeoQuEST grant from UOW. The authors would like to thank Mark Reed and Ben Williamson for sharing samples as well as Axel Müller and Jon Blundy for their constructive reviews.

References

Ackerson, M.R., Tailby, N.D., and Watson, E.B. (2015) Trace elements in quartz shed light on sediment provenance. Geochemistry Geophysics Geosystems, 16, 1894–1904.

Alberts, D., Von Werra, L., Oestlund, F., Rohner, U., Hohl, M., Michler, J., and Whitby, J.A. (2014) Design and performance of two orthogonal extraction time-of-flight secondary ion mass spectrometers for focused ion beam instruments. Instrumentation Science and Technology, 42, 432–445.

Baker, E.M., and Andrew, A.S. (1991) Geologic, fluid inclusion, and stable isotope studies of the gold- bearing Breccia Pipe at Kidston, Queensland, Australia. Economic Geology, 86, 810–

570 830.

571 Bernet, M., and Bassett, K. (2005) Provenance Analysis by Single-Quartz-Grain SEM-
572 CL/Optical Microscopy. Journal of Sedimentary Research, 75, 492–500.

573 Breiter, K., Ďurišová, J., and Dosbaba, M. (2017) Quartz chemistry – A step to understanding
574 magmatic-hydrothermal processes in ore-bearing granites: Cínovec/Zinnwald Sn-W-Li
575 deposit, Central Europe. Ore Geology Reviews, 90, 25–35.

576 Cernuschi, F., Dilles, J.H., Grocke, S.B., Valley, J.W., Kitajima, K., and Tepley, F.J. (2018)
577 Rapid formation of porphyry copper deposits evidenced by diffusion of oxygen and
578 titanium in quartz. Geology, 46, 611–614.

579 Chenery, S., and Cook, J.M. (1993) Determination of rare earth elements in single mineral grains
580 by laser ablation microprobe-inductively coupled plasma mass spectrometry-preliminary
581 study. Journal of Analytical Atomic Spectrometry, 8, 299–303.

582 Dennen, W.H. (1967) Trace elements in quartz as indicators of provenance. Geological Society
583 of America Bulletin, 78, 125–130.

584 Ebert, S.W., and Rye, R.O. (1997) Secondary Precious Metal Enrichment by Steam-Heated
585 Fluids in the Crofoot-Lewis Hot Spring Gold-Silver Deposit and Relation to Palaeoclimate.
586 Economic Geology, 92, 578–600.

587 Gaillou, E., Post, J.E., Rost, D., and Butler, J.E. (2012) Boron in natural type IIb blue diamonds:
588 Chemical and spectroscopic measurements. American Mineralogist, 97, 1–18.

589 Götze, J. (2009) Chemistry, textures and physical properties of quartz – geological interpretation
590 and technical application. Mineralogical Magazine, 73, 645–671.

591 Götze, J., and Zimmerle, W. (2000) Quartz and silica as guide to provenance in sediments and
592 sedimentary rocks: Contributions to Sedimentary Geology 21, 91 p.

593 Lafuente, B., Downs, R.T., Yang, H., and Stone, N. (2015) The power of databases: The RRUFF
594 project, 1–29 p. (T. Armbruster & R.M. Danisi, Eds.)Highlights in Mineralogical
595 Crystallography. W. De Gruyter, Berlin, Germany.
596 Larsen, R.B., Henderson, I., Ihlen, P.M., and Jacamon, F. (2004) Distribution and petrogenetic
597 behaviour of trace elements in granitic pegmatite quartz form South Norway. Contributions
598 to Mineralogy and Petrology, 147, 615–628.
599 Lynne, B.Y., Campbell, K.A., James, B.J., Browne, P.R.J., and Moore, J. (2007) Tracking
600 crystallinity in siliceous hot-spring deposits. American Journal of Science, 307, 612–641.
601 McCubbin, F.M., Steele, A., Nekvasil, H., Schnieders, A., Rose, T., Fries, M., Carpenter, P.K.,
602 and Jolliff, B.L. (2010) Detection of structurally bound hydroxyl in fluorapatite from
603 Apollo Mare basalt 15058,128 using TOF-SIMS. American Mineralogist, 95, 1141–1150.
604 Monnier, L., Lach, P., Salvi, S., Melleton, J., Bailly, L., Béziat, D., Monnier, Y., and Gouy, S.
605 (2018) Quartz trace-element composition by LA-ICP-MS as proxy for granite
606 differentiation, hydrothermal episodes, and related mineralization: The Beauvoir Granite
607 (Echassières district), France. Lithos, 320–321, 355–377.
608 Montalvo, S.D., Reddy, S.M., Saxey, D.W., Rickard, W.D.A., Fougerouse, D., Quadir, Z., and
609 Johnson, T.E. (2019) Nanoscale constraints on the shock-induced transformation of zircon
610 to reidite. Chemical Geology, 507, 85–95.
611 Müller, A., and Knies, J. (2013) Trace elements and cathodoluminescence of detrital quartz in
612 Arctic marine sediments – A new ice-rafted debris provenance proxy. Climate of the
613 Past, 9, 2615–2630.
614 Müller, A., and Koch-Müller, M. (2009) Hydrogen speciation and trace element contents of
615 igneous, hydrothermal and metamorphic quartz from Norway. Mineralogical Magazine, 73,

569–583.

Müller, A., Lennox, P., and Trzebski, R. (2002) Cathodoluminescence and micro-structural evidence for crystallisation and deformation processes of granites in the Eastern Lachlan Fold Belt (SE Australia). Contributions to Mineralogy and Petrology, 143, 510–524.

Müller, A., Wiedenbeck, M., van den Kerkhof, A.M., Kronz, A., and Simon, K. (2003) Trace elements in quartz – a combined electron microprobe, secondary ion mass spectrometry, laser-ablation ICP-MS, and cathodoluminescence study. European Journal of Mineralogy, 15, 747–763.

Müller, A., Ihlen, P.M., and Kronz, A. (2008) Quartz chemistry in polygeneration Sveconorwegian pegmatites, Froland, Norway. European Journal of Mineralogy, 20, 447–463.

Müller, A., van den Kerkhof, A.M., Behr, H.-J., Kronz, A., and Koch-Müller, M. (2010) The evolution of late-Hercynian granites and rhyolites documented by quartz - A review, 185–204 p. Earth and Environmental Science Transactions of the Royal Society of Edinburgh Vol. 100.

Müller, A., Herklotz, G., and Giegling, H. (2018) Chemistry of quartz related to the Zinnwald/Cínovec Sn-W-Li greisen-type deposit, Eastern Erzgebirge, Germany. Journal of Geochemical Exploration, 190, 357–373.

Pabst, S., Zack, T., Savov, I.P., Ludwig, T., Rost, D., and Vicenzi, E.P. (2011) Evidence for boron incorporation into the serpentine crystal structure. American Mineralogist, 96, 1112–1119.

Penniston-Dorland, S.C. (2001) Illumination of vein quartz textures in a porphyry copper ore deposit using scanned cathodoluminescence: Grasberg Igneous Complex, Irian Jaya,

639 Indonesia. American Mineralogist, 86, 652–666.

640 Perny, B., Eberhardt, P., Ramseyer, K., Mullis, J., and Pankrath, R. (1992) Microdistribution of
641 Al, Li, and Na in α quartz: possible causes and correlation with short-lived
642 cathodoluminescence. American Mineralogist, 77, 534–544.

643 Peterková, T., and Dolejš, D. (2019) Magmatic-hydrothermal transition of Mo-W-mineralized
644 granite-pegmatite-greisen system recorded by trace elements in quartz: Krupka district,
645 Eastern Krušné hory/Erzgebirge. Chemical Geology.

646 Rubanov, S., and Munroe, P.R. (2004) FIB-induced damage in silicon. Journal of Microscopy,
647 214, 213–221.

648 Rusk, B., Koenig, A., and Lowers, H. (2011) Visualizing trace element distribution in quartz
649 using cathodoluminescence, electron microprobe, and laser ablation-inductively coupled
650 plasma-mass spectrometry. American Mineralogist, 96, 703–708.

651 Rusk, B.G., Reed, M.H., Dilles, J.H., and Kent, A.J.R. (2006) Intensity of quartz
652 cathodoluminescence and trace-element content in quartz from the porphyry copper deposit
653 at Butte, Montana. American Mineralogist, 91, 1300–1312.

654 Rusk, B.G., Lowers, H.A., and Reed, M.H. (2008) Trace elements in hydrothermal quartz:
655 Relationships to cathodoluminescent textures and insights into vein formation. Geology, 36,
656 547–550.

657 Saunders, K., Rinnen, S., Blundy, J., Dohmen, R., Klemme, S., and Arlinghaus, H.F. (2012)
658 TOF-SIMS and electron microprobe investigations of zoned magmatic orthopyroxenes:
659 First results of trace and minor element analysis with implications for diffusion modeling.
660 American Mineralogist, 97, 532–542.

661 Seitz, S., Putlitz, B., Baumgartner, L., Meibom, A., Escrig, S., and Bouvier, A.S. (2018) A

662 NanoSIMS Investigation on Timescales Recorded in Volcanic Quartz From the Silicic
663 Chon Aike Province (Patagonia). Frontiers in Earth Science, 6, 1–19.
664 Seyedolali, A., Krinsley, D.H., Boggs, S., O'Hara, P.F., Dypvik, H., and Goles, G.G. (1997)
665 Provenance interpretation of quartz by scanning electron microscope–cathodoluminescence
666 fabric analysis. Geology, 25, 787–790.
667 Sprunt, E.S. (1981) Causes of quartz cathodoluminescence colors. In O. Johari, Ed., Scanning
668 Electron Microsccopy, Part 1 pp. 525–530. Scanning Microscopy International, Chicago.
669 Stevens-Kalceff, M.A. (2009) Cathodoluminescence microcharacterisation of point defects in α-
670 quartz. Minerological Magazine, 73, 585–605.
671 Tanner, D., Henley, R.W., Mavrogenes, J.A., and Holden, P. (2013) Combining in situ isotopic,
672 trace element and textural analyses of quartz from four magmatic-hydrothermal ore
673 deposits. Contributions to Mineralogy and Petrology, 166, 1119–1142.
674 Taylor, S.R., and McLennan, S. (1985) Continental crust: its composition and evolution. An
675 examination of the geochemical record preserved in sedimentary rocks. Oxford, Blackwell
676 Scientific, 312 pp.
677 Varnes, D.J. (1963) Geology and Ore Deposits of the South Silverton Mining Area, San Juan
678 County, Colorado.
679 Vasyukova, O. V., Goemann, K., Kamenetsky, V.S., MacRae, C.M., and Wilson, N.C. (2013)
680 Cathodoluminescence properties of quartz eyes from porphyry-type deposits: Implications
681 for the origin of quartz. American Mineralogist, 98, 98–109.
682 Wark, D.A., and Watson, E.B. (2006) TitaniQ: A titanium-in-quartz geothermometer.
683 Contributions to Mineralogy and Petrology, 152, 743–754.
684 Weil, J.A. (1984) A review of electron spin spectroscopy and its application to the study of

paramagnetic defects in crystalline quartz. Physics and Chemistry of Minerals, 10, 149–165.

Whitby, J.A., Östlund, F., Horvath, P., Gabureac, M., Riesterer, J.L., Utke, I., Hohl, M., Sedláček, L., Jiruše, J., Friedli, V., and others (2012) High Spatial Resolution Time-of-Flight Secondary Ion Mass Spectrometry for the Masses: A Novel Orthogonal ToF FIB-SIMS Instrument with In Situ AFM. Advances in Materials Science and Engineering, 2012, 1–13.

List of figure captions

Figure 1. Optical images of studied samples with approximate TOF-SIMS analysis locations labelled: (**a**) EPI-CS, cryptocrystalline silica from an epithermal deposit, (**b**) EPI-Q, microcrystalline quartz from an epithermal sinter, (**c**) GREI-Q, fractionated high-temperature quartz from a greisen associated with cassiterite, and (**d**) UST-Q, the most magmatic end-member of hydrothermal quartz from the carapace of a magma chamber, where qtz = quartz, apl = aplite, cas = cassiterite, adl = adularia, py = pyrite, csi = cryptocrystalline silica and (res) = casting resin.

Figure 2. Schematic environments of crystallisation in a magmatic-hydrothermal system for each sample, where C = EPI-CS, E = EPI-Q, G = GREI-Q, and U = UST-Q.

Figure 3. Representative Z-section clipped from the three-dimensional stack of two-dimensional isotope maps to eliminate anomalies from the gold coating and surface defects, but not so deep that sample charging anomalies are present.

708

709 **Figure 4.** Series of boxplots showing the range and distribution of elements measured by LA-
710 ICP-MS in the four samples ordered by decreasing median value. The data gives an indication of
711 the overall geochemistry of each sample. `

712

713 **Figure 5.** Positive correlation between the ∑1+ and ∑3+ cations partitioned in quartz and silica.
714 Note that in quartz, the ∑1+ and ∑3+ cations in quartz fall along a consistent trend, while
715 cryptocrystalline silica hosts a greater proportion of the ∑1+ cations.

716

717 **Figure 6.** Panchromatic CL images of samples highlighting characteristic textures: (**a**) EPI-CS
718 showing successive botryoidal zones with variable CL intensity, (**b**) EPI-Q hosting high-contrast,
719 euhedral oscillatory zones, (**c**) GREI-Q showing oscillatory and sector zoning cross-cut by a
720 patchy, dark micro-vein network, and (**d**) UST-Q also showing an irregular network of darker
721 micro-veins cross-cutting weaker oscillatory and sector zones. These CL images are
722 representative of internal textures but do not spatially correlate to TOF-SIMS analysis areas.

723

724 **Figure 7.** Qualitative isotope maps for ^{28}Si, ^{27}Al, ^{23}Na, ^{7}Li, ^{40}Ca and ^{39}K in the EPI-CS sample.
725 Positively correlated high concentrations Al, Na, K, and Ca are present in irregular, sporadic
726 clusters, highlighted by the arrow labelled '1'. Aluminium, K, Li, and Na are present in a
727 botryoidal lamination, highlighted by the arrow labelled '2'. The scale applies to each image in
728 panel.

729

730 **Figure 8.** Qualitative isotope maps for ^{28}Si, ^{27}Al, ^{23}Na, ^{7}Li, ^{40}Ca and ^{39}K for the EPI-Q sample.
731 Euhedral, oscillatory zoning predominately controls trace element distribution. Within single
732 oscillatory zones of K, concentrations are variable, especially in parts indicated by the arrows
733 labelled '1'. Silicon voids host Al, Na, K, and Ca as surface contamination, but not Li. A small
734 area at the top of isotope maps is an overlap with another TOF-SIMS ablation area and is not
735 inherent to the crystal, indicated by the arrow labelled '2' in the Si map. The scale applies to
736 each image in panel.
737
738 **Figure 9.** Qualitative isotope maps for ^{28}Si, ^{27}Al, ^{23}Na, ^{7}Li, ^{40}Ca and ^{39}K for the GREI-Q sample.
739 Trace elements are distributed in a mosaic-like texture, with high concentrations of K, Na, Ca
740 from surface contamination in Si voids. High concentrations of Al and Li are positively
741 correlated with Si. Spherical areas of high Al and K, indicated by the dashed arrows labelled '1',
742 differ from other Si voids as they do not host Na, Ca or Li. Vignetting is apparent in Si and Al
743 maps due to detector falloff at this analysis scale. The scale applies to each image in panel.
744
745 **Figure 10.** Qualitative isotope maps for ^{28}Si, ^{27}Al, ^{23}Na, ^{7}Li, ^{40}Ca and ^{39}K for the UST-Q sample.
746 Nanometer-scale clusters of high concentration correlate in Al and K. An example is highlighted
747 by the arrows labelled '1' in the Al and K maps. Nano-cluster-absent micro-veins are highlighted
748 by solid lines, and variable abundance of nano-clusters are separated by a dashed line in the same
749 maps. Microscale clusters associated with surface defects are present in Al, Na, Ca and K, an
750 example highlighted by arrows labelled '2'. Anomalous faint lineation in Na and Ca is partially
751 traced by white solid lines in the Na map. Calcium-deficient veins do not correlate to Al and K
752 deficient veins. The scale applies to each image in panel.

753

754 **Figure 11.** High spatial resolution (50 μm width) qualitative isotope maps for ^{28}Si, ^{27}Al, ^{23}Na,
755 ^{7}Li, ^{40}Ca and ^{39}K for the UST-Q sample. Aluminium, Na, Ca and K from polishing media residue
756 are concentrated in micrometer scale cracks and nanometer scale Si-deficient areas. Correlating
757 Al and K nano-clusters, indicated by the arrows in Al and K maps, may also originate from
758 surface contamination but still highlight the fine spatial resolution of TOF-SIMS. Lithium was
759 not resolved in this sample at this scale. The scale applies to each image in panel.

760

761 **Figure 12.** Relative proportion of the monovalent cations balancing Al^{3+} in silica samples
762 assuming a three-component system (K, Li, and Na). Li^{+} acts as the dominant charge balancing
763 ion in EPI-Q while K^{+} is predominant in the more magmatic end-member UST-Q.

764

765 **Figure 13.** Comparison of pixel intensity values in panchromatic CL and TOF-SIMS images for
766 paired transects in the EPI-Q sample. While Al does not vary considerably over alternating light
767 and dark CL zones (gray bands behind graphs), the relative proportion of charge balancing ions
768 (such as K, Li and Na) broadly increases. Note the spike in Al around 80 μm and Ca around 110
769 μm are associated with Si-voids.

770

771 **Figure 14.** BSE images comparing TOF-SIMS ablation grids in quartz resulting from (**a**) a well-
772 focussed beam with optimum spot size to step size ratio, (**b**) a poorly-focussed ion beam with
773 spots too close together resulting in inaccurate data, and (**c**) a collapsed mineral surface resulting
774 from the TOF-SIMS beam current too high per unit area.

775

Table 1 – Summary statistics for element concentrations (ppm) from a LA-ICP-MS traverse in each sample

	EPI-CS				EPI-Q				GREI-Q				UST-Q			
	Min	**Max**	**Range**	**Median**	**Min**	**Max**	**Range**	**Median**	**Min**	**Max**	**Range**	**Median**	**Min**	**Max**	**Range**	**Median**
Ag	*b.d.*	796.8	796.8	*b.d.*	*b.d.*	113.9	113.9	2.71	*b.d.*	67.30	67.30	0.65	*b.d.*	64.10	64.07	0.66
Al	1.45	3638	3637	217.7	3009	6212	3203	4149	*b.d.*	608.1	607.6	201.3	254.1	7691	7437	562.8
As	*b.d.*	10.73	10.73	1.10	*b.d.*	3.02	2.98	0.91	*b.d.*	15.00	14.97	0.88	*b.d.*	5.40	5.34	0.84
B	*b.d.*	24.89	24.81	9.04	*b.d.*	17.25	17.06	2.42	*b.d.*	56.93	56.74	5.90	*b.d.*	14.49	14.48	4.08
Ba	*b.d.*	22.31	22.30	0.52	4.94	24.35	19.41	12.57	*b.d.*	*b.d.*	*b.d.*	*b.d.*	*b.d.*	17.25	17.24	0.51
Be	*b.d.*	21.74	21.55	8.83	*b.d.*	4.35	4.24	0.95	*b.d.*	4.95	4.57	0.62	*b.d.*	2.74	2.33	0.51
Ca	*b.d.*	1108	1108	124.7	*b.d.*	788.2	788.1	131.5	*b.d.*	630.8	630.8	103.8	3.29	624.2	620.9	78.89
Ce	*b.d.*	26.18	26.18	*b.d.*	*b.d.*	2.53	2.53	*b.d.*	*b.d.*	1.43	1.42	*b.d.*	*b.d.*	1.70	1.69	*b.d.*
Cs	*b.d.*	120.6	120.3	1.52	1.34	10.20	8.86	3.57	*b.d.*	6.57	6.56	*b.d.*	*b.d.*	1.00	0.99	*b.d.*
Cu	*b.d.*	25.63	25.62	0.95	*b.d.*	9.98	9.92	2.01	*b.d.*	3.93	3.82	0.74	*b.d.*	4.22	4.12	0.75
Ge	*b.d.*	5.07	5.06	1.50	*b.d.*	4.34	4.34	1.82	*b.d.*	7.74	7.72	2.14	*b.d.*	5.17	5.17	1.27
K	3.78	1059	1055	118.0	110.8	1135	1024	370.5	1.02	113.1	112.1	18.28	83.45	4232	4149	260.8
Li	*b.d.*	14.38	14.38	2.67	116.5	409.7	293.2	284.1	1.31	64.22	62.91	14.49	*b.d.*	4.41	4.40	0.55
Mg	1.89	342.1	340.2	5.90	1.77	245.4	243.6	12.11	*b.d.*	23.89	23.86	0.82	0.94	433.7	432.7	4.82
Mn	1.03	77.31	76.28	3.25	2.66	649.9	647.3	10.44	*b.d.*	20.74	20.74	*b.d.*	*b.d.*	63.41	63.25	2.54
Na	2.35	975.0	972.6	130.5	*b.d.*	302.7	302.4	81.16	0.96	383.6	382.6	55.88	*b.d.*	337.1	337.1	65.82
Rb	*b.d.*	47.92	47.77	1.53	2.15	20.52	18.37	6.00	*b.d.*	2.25	2.25	*b.d.*	*b.d.*	37.24	37.24	*b.d.*
Sb	*b.d.*	38.59	38.29	8.08	5.30	46.36	41.06	11.66	*b.d.*	*b.d.*	*b.d.*	*b.d.*	*b.d.*	1.45	1.44	*b.d.*
Se	*b.d.*	7.51	7.50	1.34	*b.d.*	6.63	6.61	1.26	*b.d.*	7.79	7.72	1.96	*b.d.*	17.92	17.78	2.47
Sn	*b.d.*	17.46	17.46	*b.d.*	*b.d.*	4.35	4.34	*b.d.*	*b.d.*	2.47	2.42	*b.d.*	*b.d.*	3.89	3.84	*b.d.*
Sr	*b.d.*	39.10	39.00	0.65	8.45	48.17	39.72	18.20	*b.d.*	2.17	2.16	*b.d.*	*b.d.*	1.99	1.97	*b.d.*
Ti	*b.d.*	47.67	47.57	0.66	*b.d.*	30.69	30.56	2.03	*b.d.*	5.65	5.37	1.09	15.71	70.90	55.19	34.49
Y	*b.d.*	1.21	1.21	*b.d.*	*b.d.*	*b.d.*	*b.d.*	*b.d.*	*b.d.*	*b.d.*	*b.d.*	*b.d.*	*b.d.*	*b.d.*	*b.d.*	*b.d.*

Note: *b.d.* refers to values below the detection limit.

Table 2 – Spatial characteristics of elements along a LA-ICP-MS traverse in each sample

	Consistently above detection	Locally concentrated	Below detection
UST-Q	Al, Ba, Cs, K, Li, Mg, Mn, Na, Rb, Sn, Sr, Ti	Ag, Ce, Sb, Sn, Sr	As, B, Be, Ca, Cu, Ge, Na, Se, Y
GREI-Q	Al, As, Li	Ag, B, Ba, Be, Ce, Cs, Mg, Mn, Rb, Sn, Sr	Be, Ca, Cu, Ge, K, Na, Sb, Se, Ti, Y
EPI-Q	Ag, Al, Ba, Ce, Cs, Cu, K, Li, Mg, Na, Rb, Sb, Sr, Ti, Y	Ag, Mg, Mn, Sn, Ti	As, B, Be, Ca, Ge, Se, Y
EPI-CS	Al, B, Ba, Be, Cs, K, Li, Na, Rb, Sb, Sr	Ag, As, Ce, Cu, Mg, Mn, Sn, Ti, Y	As, B, Ca, Ge, Se

Table 3 – Nature of element partitioning in quartz samples inferred from TOF-SIMS

	Lattice incorporation	Nano- or microscale inclusions	Contamination in Si voids
EPI-CS		Al, Ca, K, Li, Na	Al, Ca, K, Na
EPI-Q	Al, Ca, K, Li, Na		Al, Ca, K, Na
GREI-Q	Al, K, Li	Al*, K*	Al, Ca, K, Na
UST-Q	Al, Ca, K, Na	Al, K	Al, Ca, K, Na

* Present in micrometer scale fluid inclusions

Figure 1

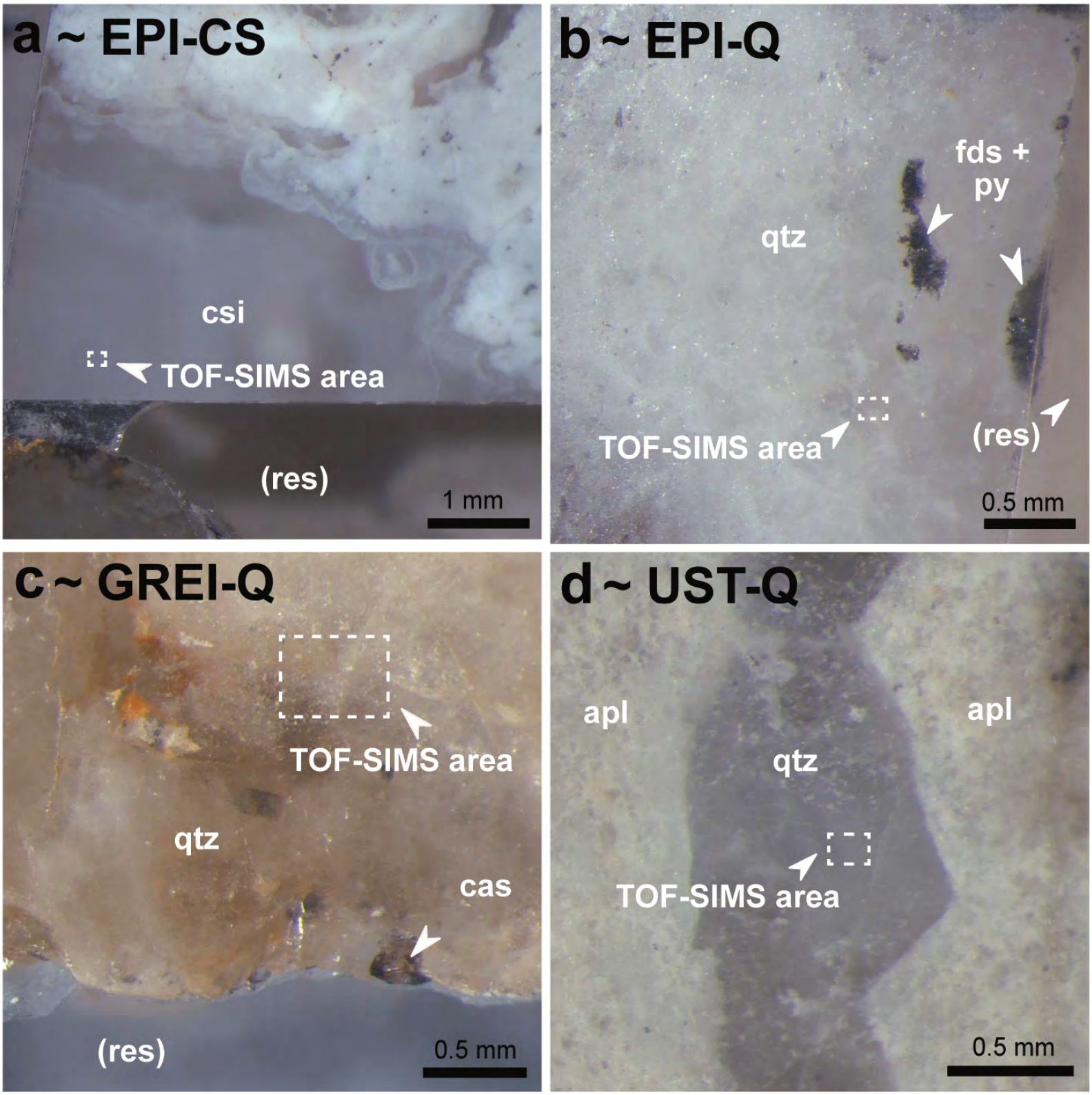
a ~ EPI-CS
csi
TOF-SIMS area
(res)
1 mm
b ~ EPI-Q
fds +
py
qtz
TOF-SIMS area
(res)
0.5 mm
c ~ GREI-Q
TOF-SIMS area
qtz
cas
(res)
0.5 mm
d ~ UST-Q
apl
apl
qtz
TOF-SIMS area
0.5 mm

Figure 2

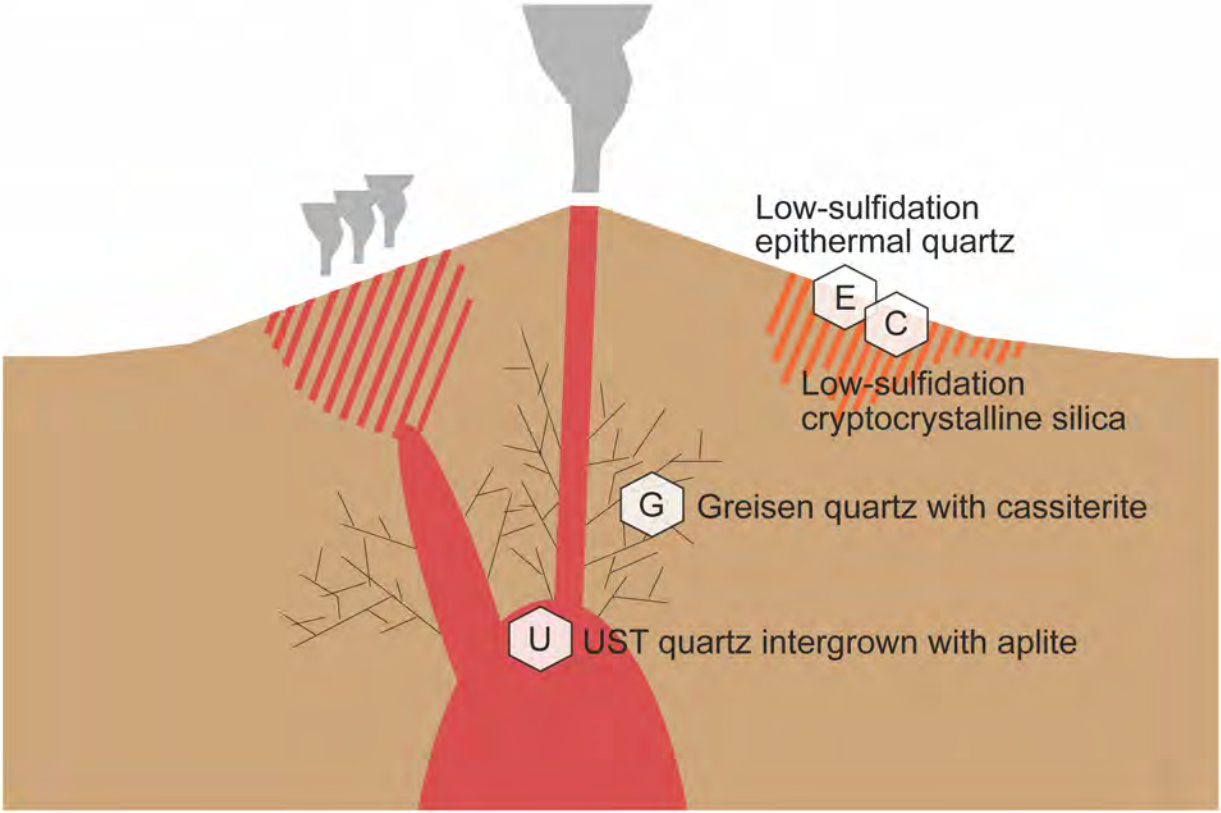
Low-sulfidation
epithermal quartz
E
C
Low-sulfidation
cryptocrystalline silica
G
Greisen quartz with cassiterite
U
UST quartz intergrown with aplite

Figure 3

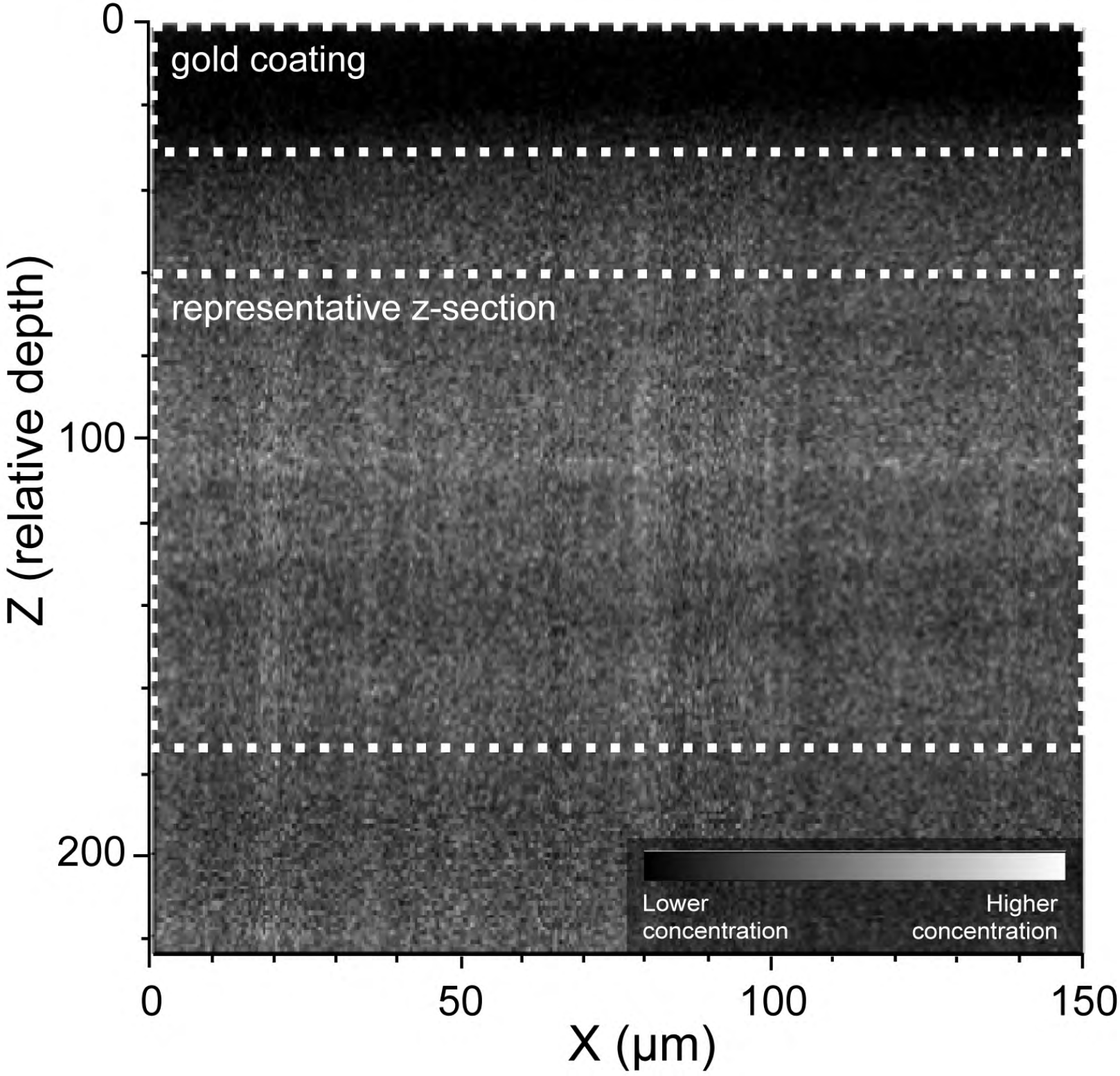
0
gold coating
representative z-section
100
200
Z (relative depth)
Lower
concentration
Higher
concentration
0
50
100
150
X (μm)

Figure 4

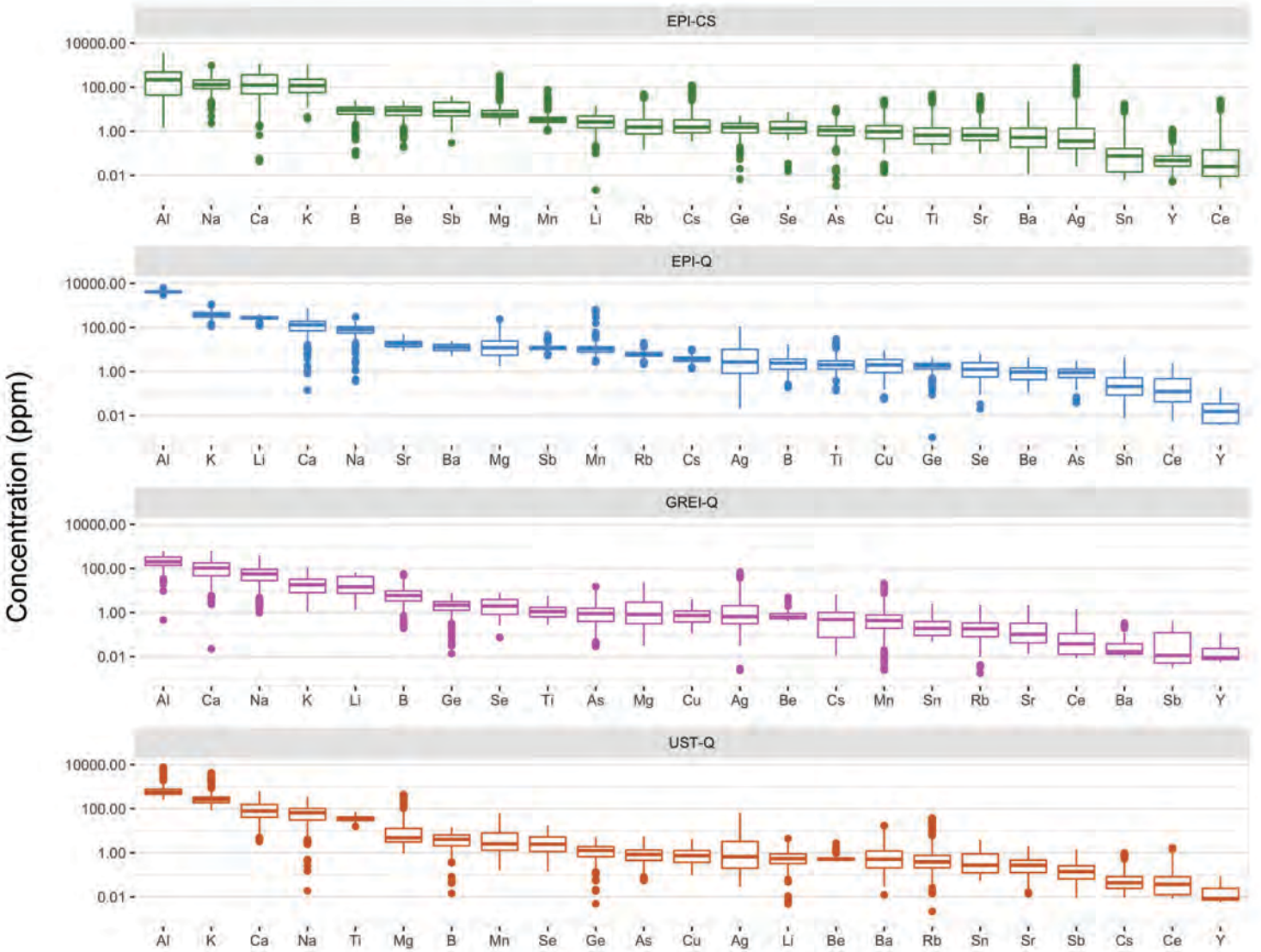
EPI-CS
10000.00
100.00
1.00
0.01
Al Na Ca K B Be Sb Mg Mn Li Rb Cs Ge Se As Cu Ti Sr Ba Ag Sn Y Ce
EPI-Q
10000.00
100.00
1.00
0.01
Al K Li Ca Na Sr Ba Mg Sb Mn Rb Cs Ag B Ti Cu Ge Se Be As Sn Ce Y
GREI-Q
10000.00
100.00
1.00
0.01
Al Ca Na K Li B Ge Se Ti As Mg Cu Ag Be Cs Mn Sn Rb Sr Ce Ba Sb Y
UST-Q
10000.00
100.00
1.00
0.01
Al K Ca Na Ti Mg B Mn Se Ge As Cu Ag Li Be Ba Rb Sn Sr Sb Cs Ce Y
Concentration (ppm)

Figure 5

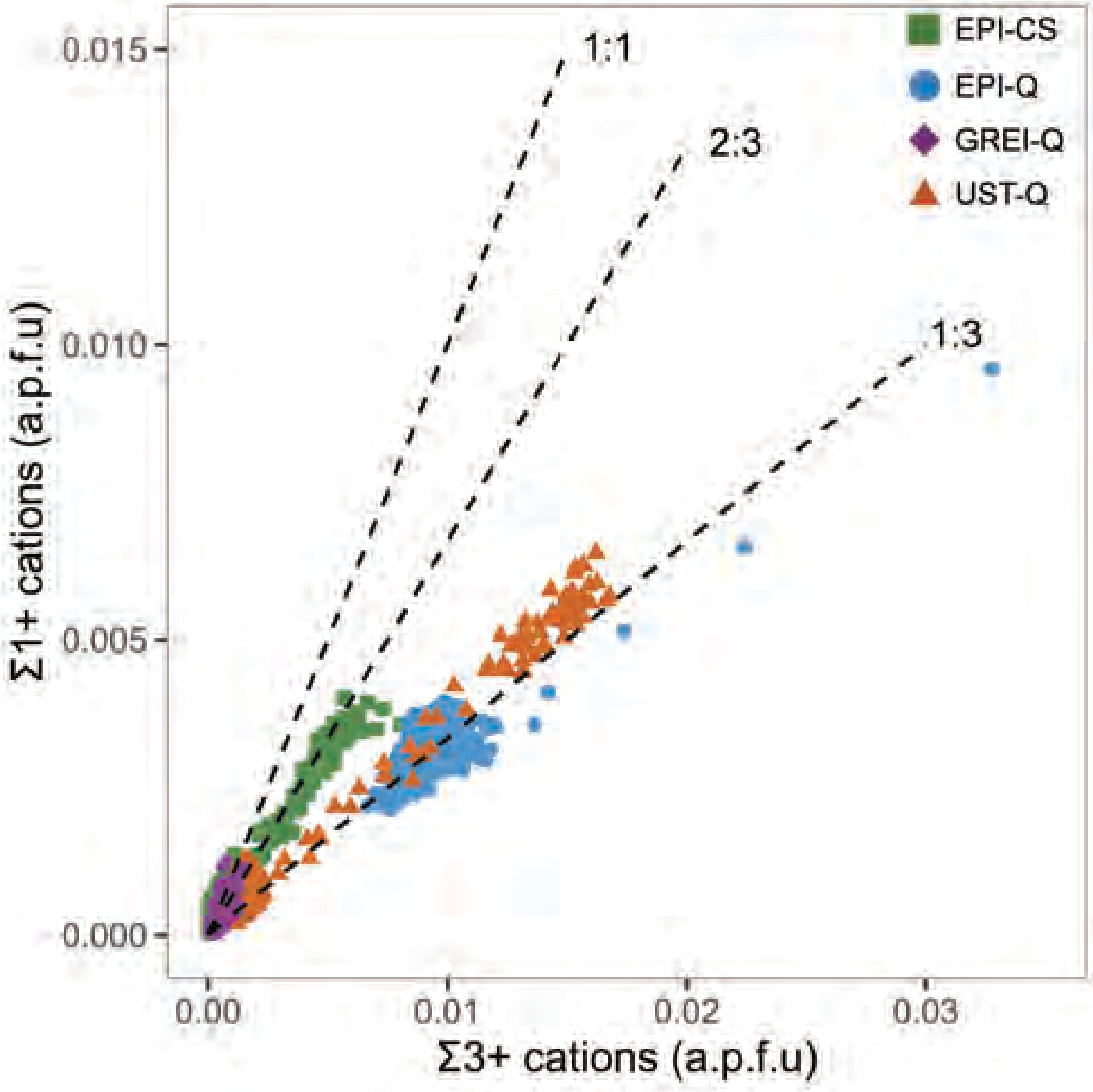
EPI-CS
EPI-Q
GREI-Q
UST-Q
1:1
2:3
1:3
0.015
0.010
0.005
0.000
Σ1+ cations (a.p.f.u)
0.00
0.01
0.02
0.03
Σ3+ cations (a.p.f.u)

Figure 6

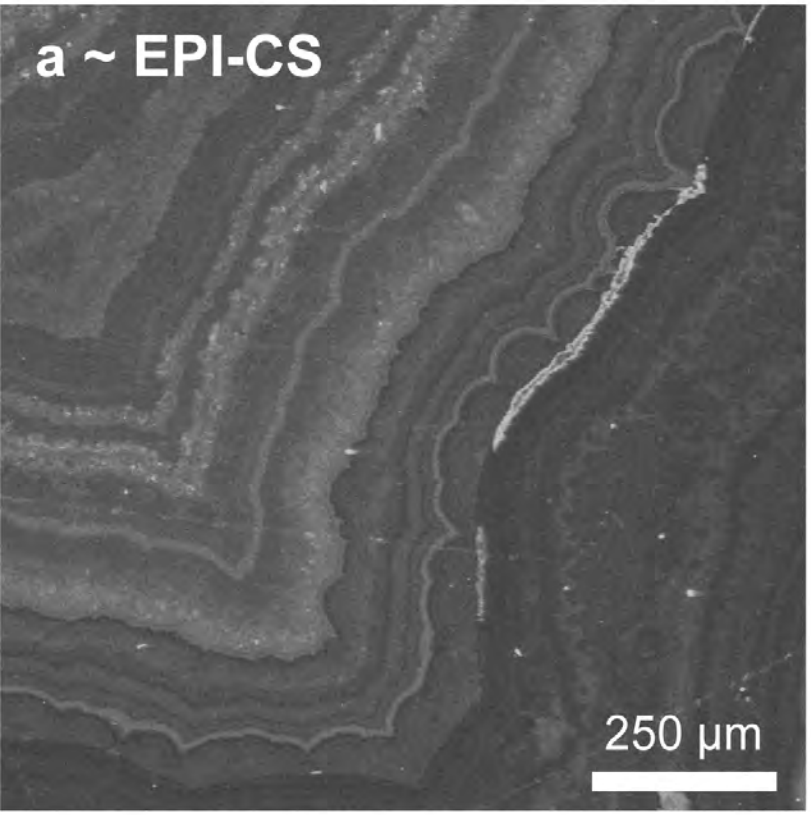

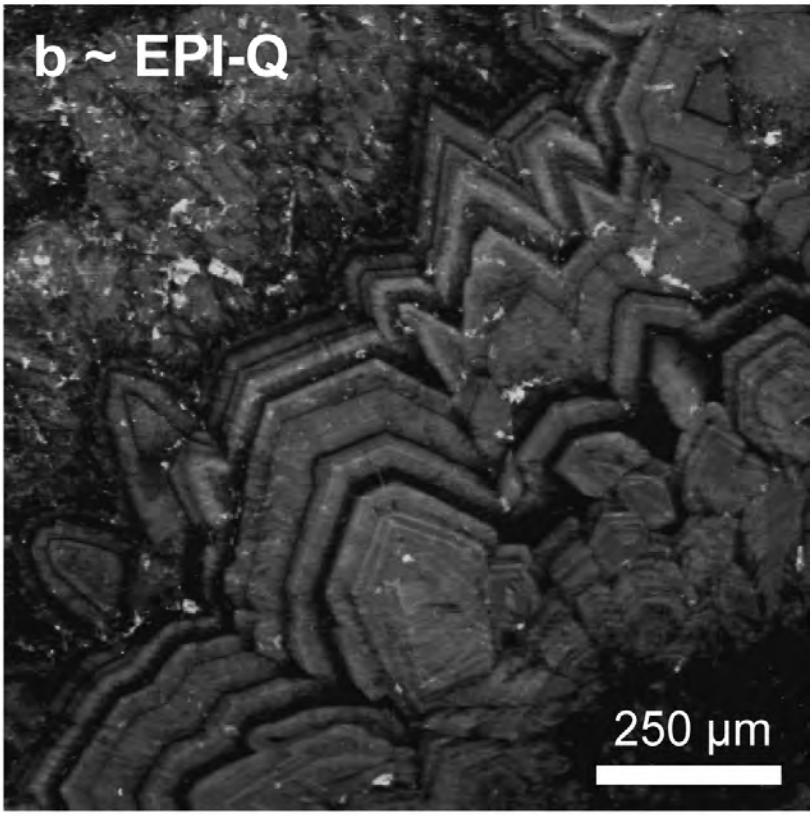

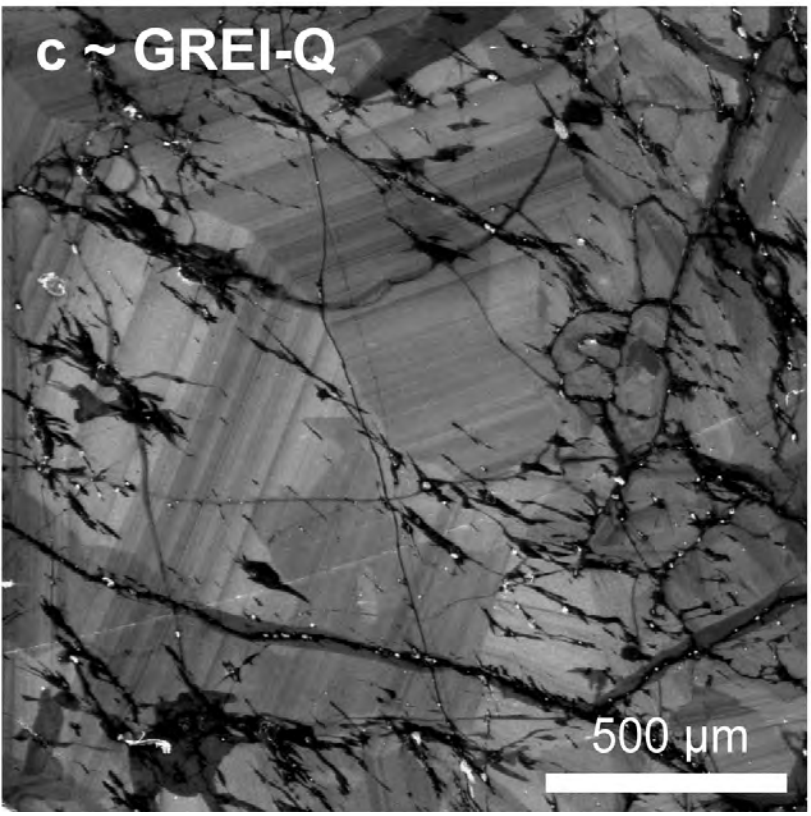

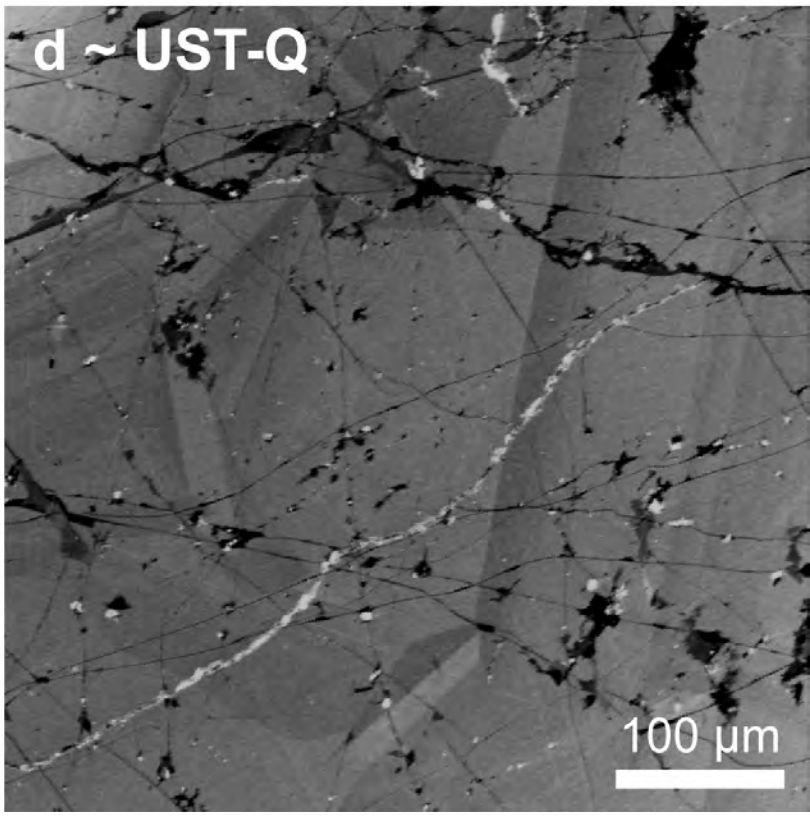

Figure 7

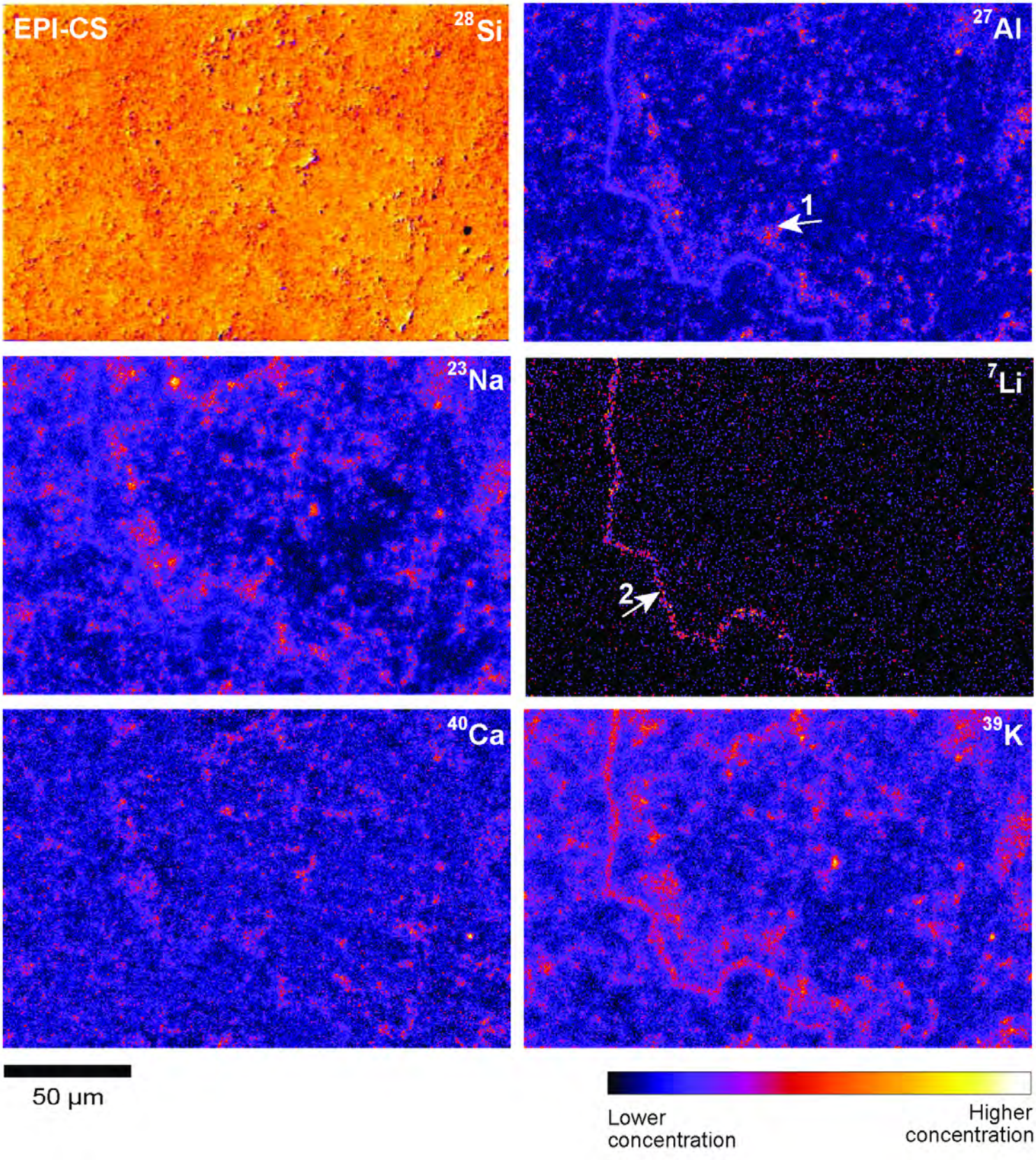
EPI-CS
^{28}Si
^{27}Al
1
^{23}Na
^{7}Li
2
^{40}Ca
^{39}K
50 µm
Lower concentration
Higher concentration

Figure 8

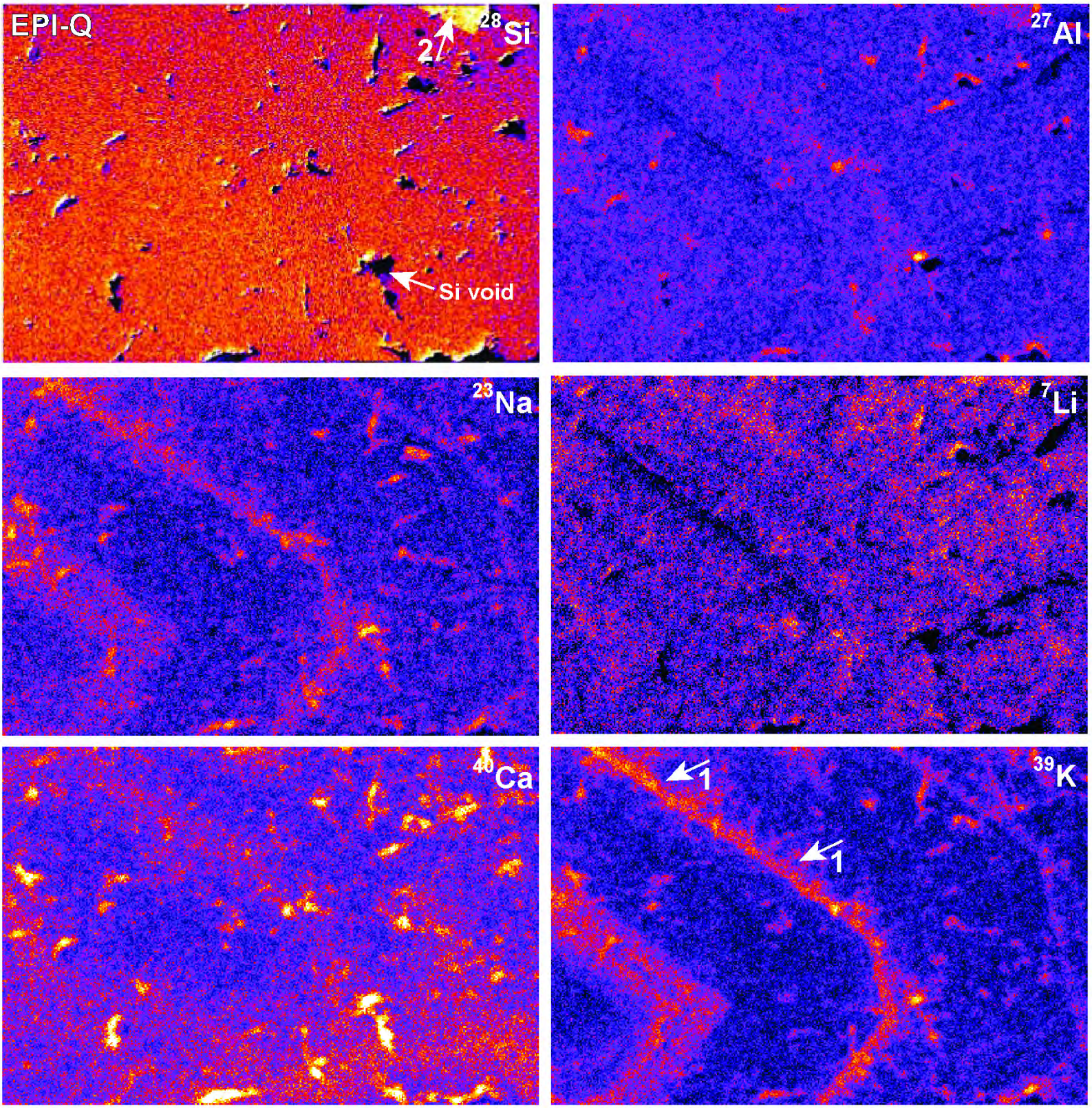
EPI-Q
28Si
2
Si void
27Al
23Na
7Li
40Ca
1
1
39K
50 µm
Lower concentration
Higher concentration

Figure 9

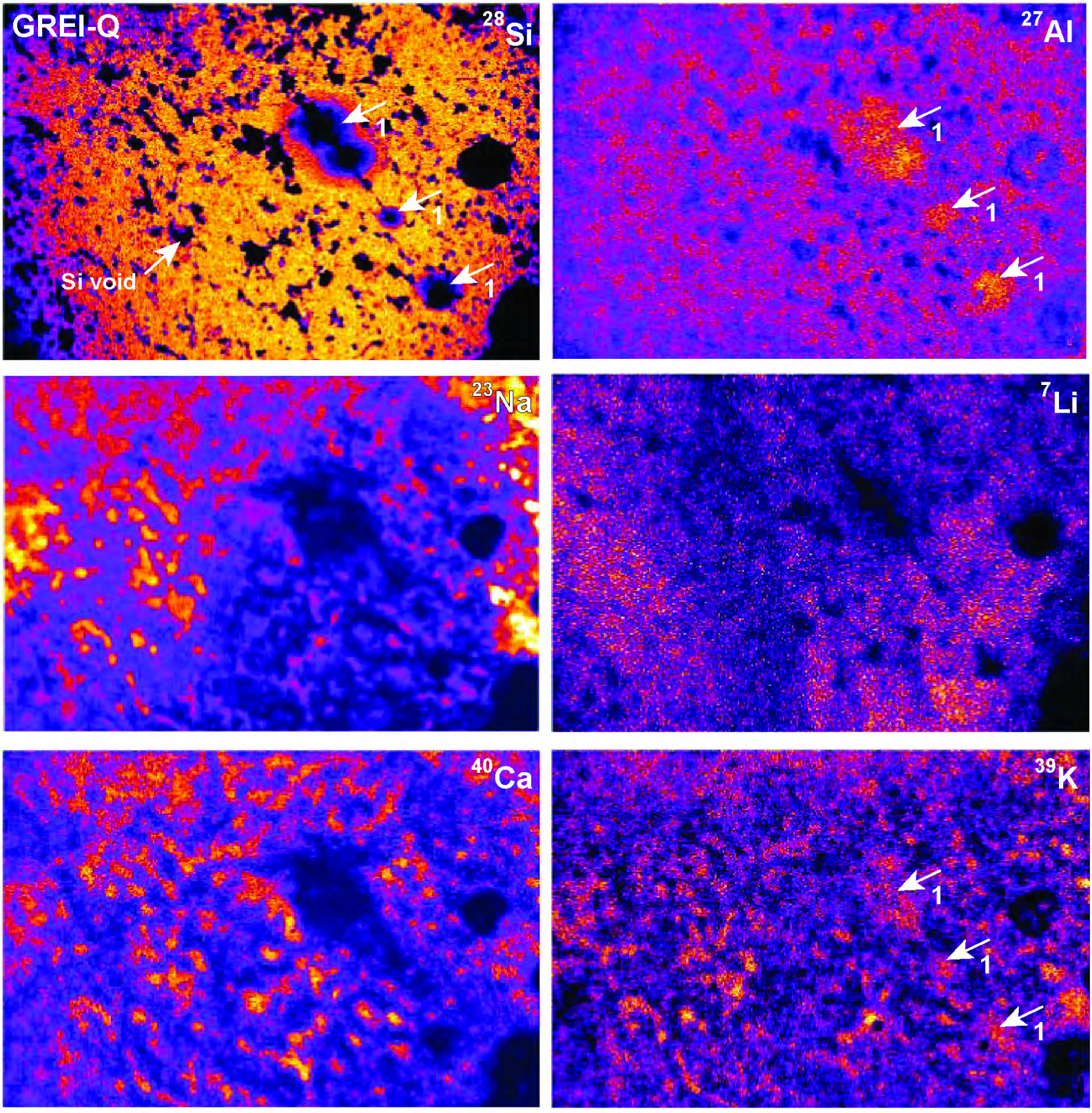
GREI-Q
^{28}Si
Si void
1
1
1
^{27}Al
1
1
1
^{23}Na
^{7}Li
^{40}Ca
^{39}K
1
1
1
125 µm
Lower concentration
Higher concentration

Figure 10

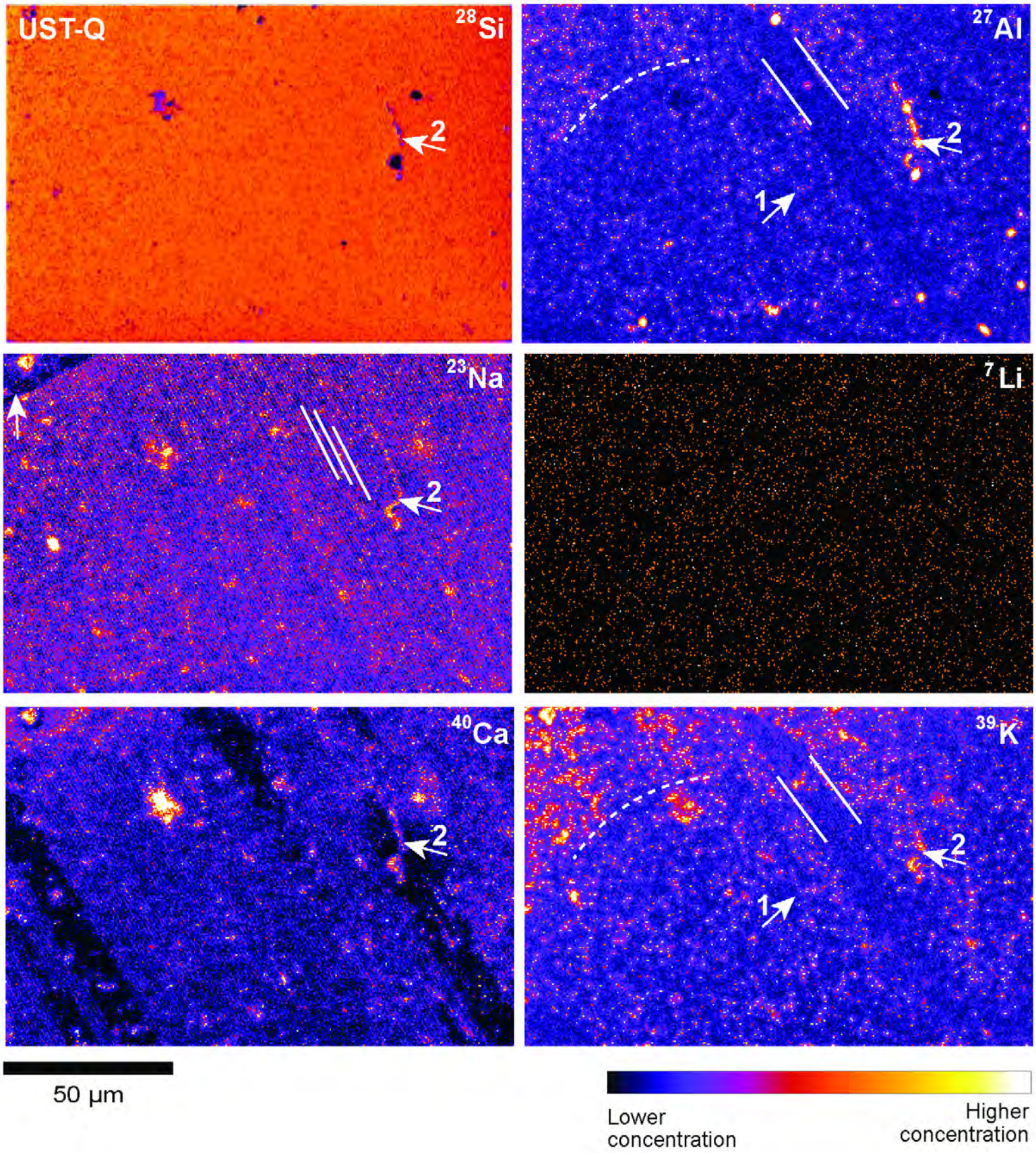
UST-Q
^{28}Si
^{27}Al
^{23}Na
^{7}Li
^{40}Ca
^{39}K
1
2
50 µm
Lower concentration
Higher concentration

Figure 11

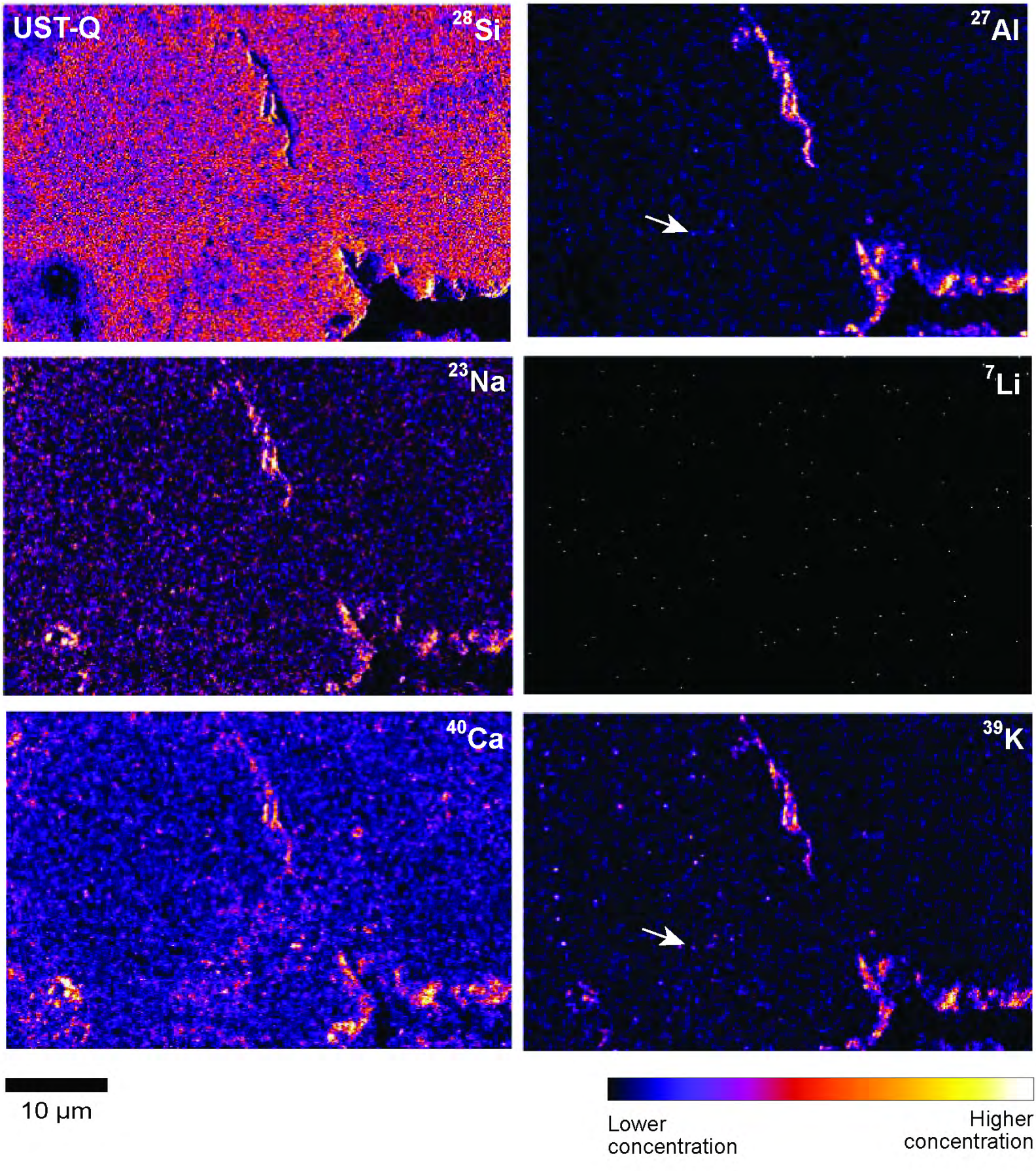
UST-Q
^{28}Si
^{27}Al
^{23}Na
^{7}Li
^{40}Ca
^{39}K
10 µm
Lower concentration
Higher concentration

Figure 12

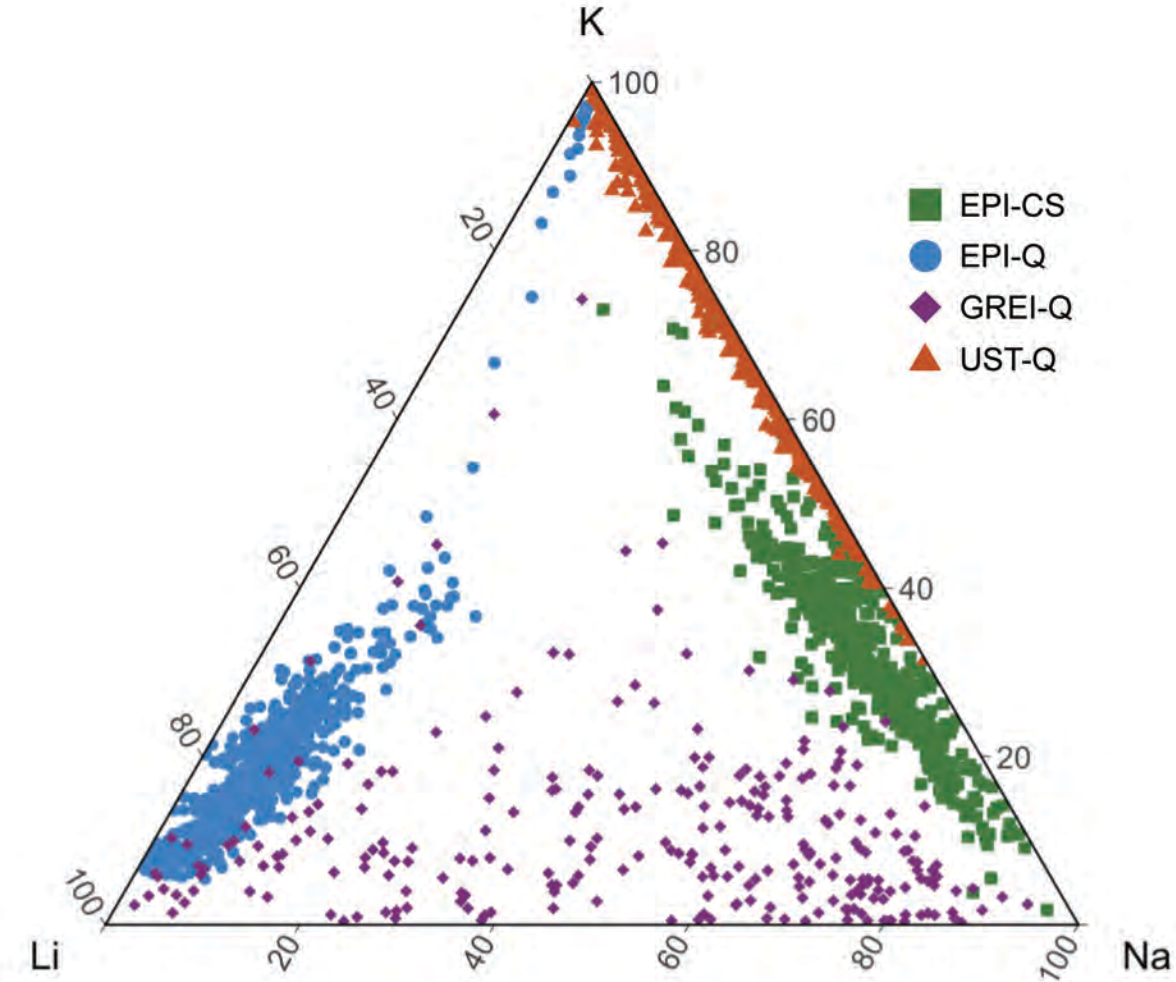

Figure 13

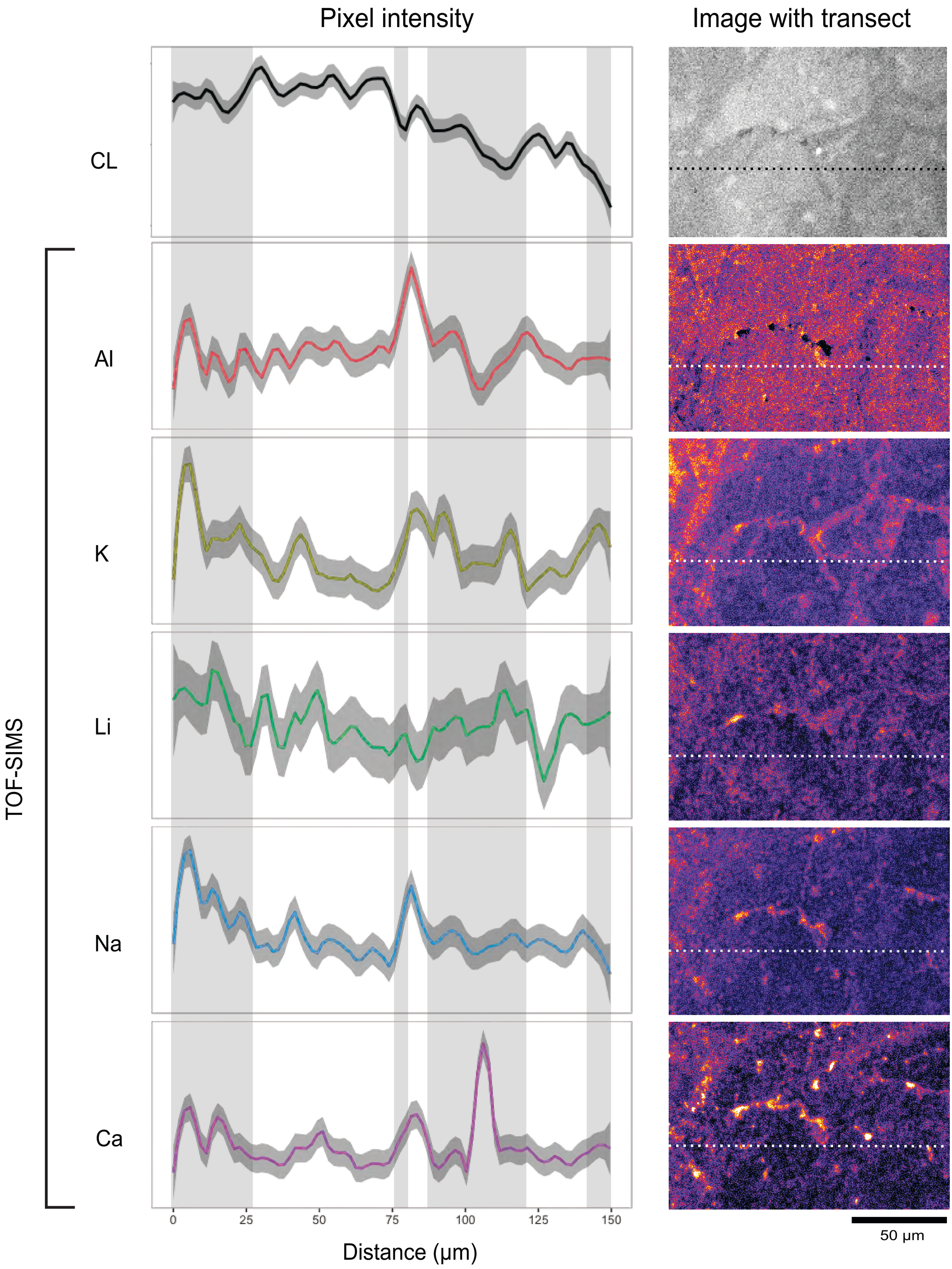
Pixel intensity
Image with transect
TOF-SIMS
CL
Al
K
Li
Na
Ca
0
25
50
75
100
125
150
Distance (μm)
50 μm

Figure 14